



OPEN Experimental investigation of the acoustic emission and energy evolution of bedded coal under uniaxial compression

Zhang Guoning¹, Yu Yongjiang²✉ & Zhang Wei³

Catastrophic events in underground coal mining usually originate from weak structures such as bedding and fractures. This study investigated the failure characteristics of coal samples with different bedding orientations by employing acoustic emission (AE) technology. Analysis of the AE time series, including ringing counts, amplitude, *b*-value, and the AF-RA relationship, was performed to characterize the failure behavior of the bedded coal. The synergistic effect of bedding and in-situ stress on the failure mechanism was also examined. The anisotropy of strain energy during the deformation and failure process was analyzed. The results indicate that bedding significantly influences the AE activity of coal during the failure process. Before failure, various AE parameters exhibit distinct precursory signals. Specifically, the sensitivity is found to be: *b*-value > cumulative ringing counts > amplitude > ringing counts. With increasing bedding orientation, the proportion of tensile cracks decreases initially, reaching a minimum at 60°. Conversely, the proportion of shear cracks exhibits an opposite trend. Microcrack development within the coal samples is primarily concentrated in the unstable crack extension and post-peak failure stage. The total strain energy, elastic strain energy, and dissipated energy display of coal sample show a V-shaped variation trend and reach their minimum values when bedding orientation is 60°. The degree of anisotropy for total strain energy, elastic strain energy, and dissipated energy exhibited a tendency to increase initially and then decrease with increasing stress. The research results can provide a scientific theoretical foundation for the stability assessment and prediction of underground mining engineering.

Keywords Bedding orientations, Uniaxial compression, Acoustic emission, Damage evolution, Energy evolution

As coal mining operations extend to greater depths, underground extraction is increasingly vulnerable to a range of geohazards, including coal wall spalling^{1,2}, roof falls^{3,4}, rock bursts^{5,6} and coal gas outbursts^{7,8} et al. These hazards often originate from localized crack initiation and propagation within the coal seam⁹. When pre-existing cracks meet the criteria for propagation, they tend to become unstable and rapidly extend within the coal mass. This unstable crack growth leads to coalescence, forming more extensive fractures that further degrade the mechanical properties and load-bearing capacity of the coal, ultimately resulting in its failure. While these events are macroscopically characterized by significant spalling or ejection of coal, the underlying failure process is closely linked to the extent of internal crack development. Coal, as a heterogeneous sedimentary rock formed through prolonged geological processes, contains numerous joints, bedding planes, and other weak structural features. Among these, bedding planes are recognized as one of the primary factors influencing the strength and failure mechanisms of the rock^{10–12}.

Numerous studies have investigated the mechanical properties, failure behavior, and crack propagation in bedded coal and rock under various loading conditions. Wang et al.^{13,14} analyzed the mechanical properties and energy evolution of bedded coal under high confining pressures. Sun et al.¹⁵ investigated the impact of bedding orientations on the fracture toughness of coal. Huang et al.¹⁶ explored the influence of bedding planes on the AE and energy evolution during coal deformation and failure. Zhou et al.¹⁷ studied the mechanical properties

¹School of Energy and Mining Engineering, China University of Mining and Technology(Beijing), Beijing 100083, China. ²School of Mining Engineering, Liaoning Technical University, Fuxin 123000, China. ³Third Geological and Mineral Exploration Institute, Gansu Geological and Mineral Bureau, Lanzhou 730000, China. ✉email: yuyongjiang001@163.com

and energy dissipation of coal samples under the combined effect of bedding planes and loading rate. Zhao et al.¹⁸ considering the conditions within deep shale reservoirs, elucidated the mechanical response and failure characteristics of shale under the coupled effects of bedding planes and high temperature. And this provided a theoretical foundation for hydraulic fracturing application in deep shale gas extraction. These studies highlight that bedding structure is a crucial factor influencing the stability of coal and rock masses. Consequently, research into the instability and failure mechanisms of bedded coal is essential for ensuring mine safety.

The AE refers to the release of elastic waves from rock under load due to the initiation, propagation, and coalescence of internal micro-cracks¹⁹. The AE is widely used to study internal damage and fracture behavior in rock materials and serves as a tool for monitoring internal state changes in rock mass. The internal damage state can be inferred by monitoring AE signals released from the rock under load^{20,21}. Liu et al.²² compared the AE characteristics of horizontally and vertically bedded coal during deformation and failure, developing a coupled damage model. Liu et al.²³ examined the mechanical properties and AE behavior of coal samples with varying bedding orientations, proposing a precursory indicator for failure. Song et al.²⁴ studied the anisotropic characteristics of AE and fractal dimension during the deformation and failure of coal with different bedding orientations. Zhang et al.²⁵ combined Brazilian tests with AE monitoring to explore the influence of bedding planes on the mechanical properties and damage modes of sandstone, suggesting that a sudden decrease in the correlation dimension of the AE time series could serve as a precursory indicator of sample failure. Furthermore, the damage and failure of rock mass involve a complex process of energy accumulation and dissipation^{26,27}. By studying the energy evolution during the deformation and failure process, a deeper understanding of rock damage, deformation and failure mechanisms can be achieved.

In conclusion, significant progress has been made in understanding the influence of bedding structure on the mechanical properties of coal. However, the comprehensively analyzing the failure mechanism of bedded coal from both AE and energy evolution perspectives remains limited. In this study, we conduct uniaxial compression tests on coal samples with four different bedding orientations (0°, 30°, 60°, and 90°), while simultaneously performing real-time AE monitoring. The relationships among stress, the AE parameters, and time are examined for the bedded coal. Additionally, the damage evolution and anisotropic characteristics of coal under the combined influence of stress and bedding planes are investigated. Furthermore, the instability and failure mechanisms of bedded coal are analyzed from an energy perspective. These findings provide a scientific basis for stability assessment and prediction in underground mine engineering.

Materials and methodology

Sample preparation

The coal samples used in this study were obtained from a longwall panel in a mine located in Ordos, Inner Mongolia, where the average coal seam thickness is 6.13 m and the average depth is 704.5 m. This coal seam has experienced numerous rock burst events during mining. Meanwhile, the coal in this mining area has a high bursting liability. Mineralogical analysis of the coal samples using X-ray diffraction revealed the following composition: 4.6% quartz, 36.4% calcite, 10.7% barite, 40.0% amorphous substance, and 8.3% clay minerals. The coal matrix contains a widespread distribution of pre-existing cracks, with evident porosity and bedding. Scanning electron microscopy (SEM) was performed on the coal samples to investigate the microstructural characteristics further, as shown in Fig. 1. The SEM images reveal the presence of numerous pores, cracks, and other weak structural features within the coal, with well-defined and evenly distributed bedding. From a microstructural perspective, these internal pores and cracks will inevitably result in significant anisotropy in the macroscopic mechanical properties of the coal. The bedding orientation (θ) is the angle between the bedding plane and the horizontal. Four groups of samples with different bedding orientations (0°, 30°, 60°, and 90°) were prepared. The collected coal blocks were prepared into standard cylindrical samples ($\varphi 50$ mm \times L100 mm) by the suggested methods of the International Society for Rock Mechanics (ISRM), ensuring that the unevenness of the upper and lower end faces is less than ± 0.05 mm and the verticality deviation is less than 0.25°. The samples were screened using a ZBL-U510 non-metallic ultrasonic tester to select samples with similar wave velocities for testing. Three samples were selected for each bedding orientation, resulting in 12 test groups. The specific mechanical parameters are listed in Table 1.

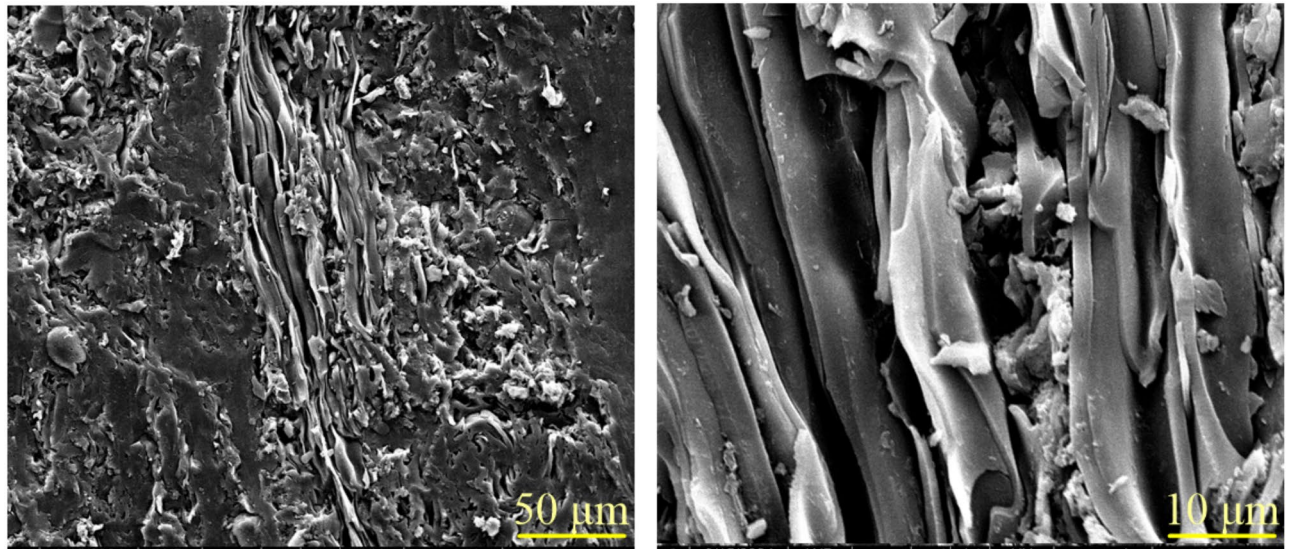
Test equipment and method

The experiments were conducted using an MTS E45.305 electro universal testing machine under displacement control at a 0.06 mm/min loading rate. A PCI-Express 8 AE monitoring system (Physical Acoustics Corporation) was employed to monitor and record AE signals during loading. The AE signal threshold was set to 40 dB, and the sampling frequency was 1 MHz. Six Nano 30 miniature probes ($\varphi 8$ mm \times 8 mm, center frequency 140 kHz) were used, with three AE probes positioned 10 mm from each end of the coal sample. Vaseline was used as a coupling to attach the AE sensors to the sample surface, and they were secured with wide rubber bands. A thin layer of vaseline was applied to the top and bottom surfaces of the sample to minimize end friction between the sample and the loading platens. The testing machine and the AE system were started synchronously at the beginning of each test to record the corresponding data. Loading was automatically terminated upon sample failure. The experimental setup is illustrated in Fig. 2.

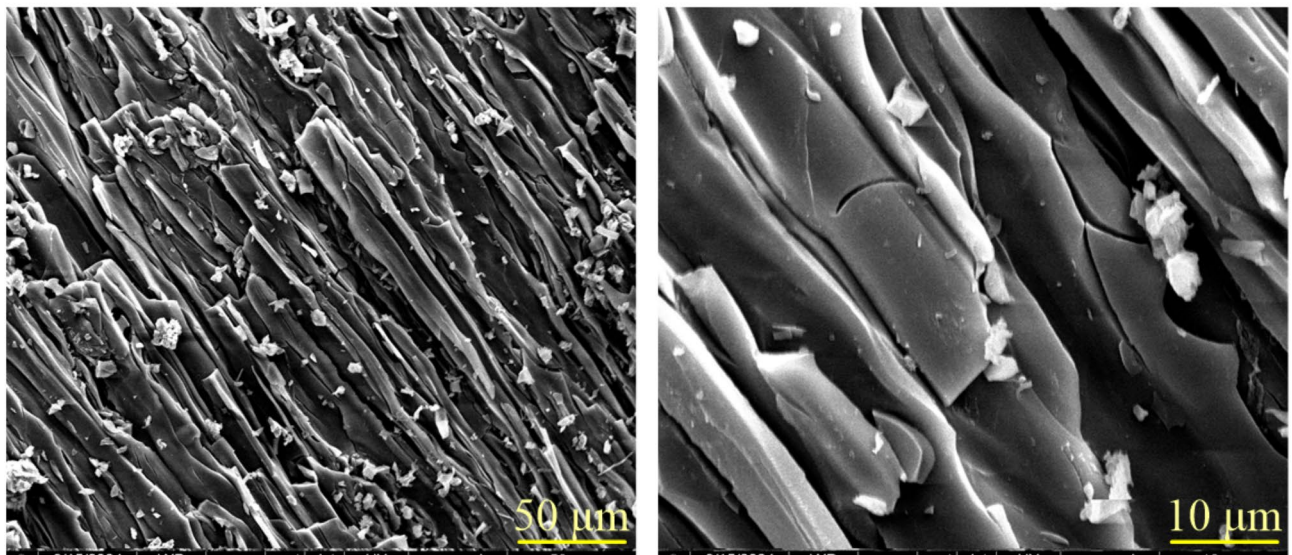
Results and discussion

Evolution of AE characteristics

During the deformation and failure process, coal releases energy through elastic waves. The ringing counts can provide real-time reflection of the internal damage characteristics of coal. Figure 3 shows the evolution of ringing counts, cumulative ringing counts, and stress with loading time for coal samples at various bedding orientations.



(a) Horizontal bedding plane



(b) Vertical bedding plane

Fig. 1. The results of scanning electron microscope (SEM).

Based on the relationship between cumulative ringing counts and axial stress, different stress thresholds were identified²⁸, as illustrated in Fig. 4. Cumulative ringing counts exhibit an approximately linear increase during both the elastic and unstable crack growth stages. The crack damage stress (σ_{cd}) is defined as the stress value at the intersection of the linear fits for these two stages. The crack closure stress (σ_{cc}) is defined as the point where the response deviates from linearity in the elastic stage. The crack initiation stress (σ_{ci}) marks the beginning of the linear elastic stage. Based on this method of identifying characteristic stress thresholds, the deformation and failure process of the coal samples was divided into five stages: crack closure stage ($0 \sim \sigma_{cc}$), linear elastic stage ($\sigma_{cc} \sim \sigma_{ci}$), stable crack growth stage ($\sigma_{ci} \sim \sigma_{cd}$), unstable crack growth stage ($\sigma_{cd} \sim \sigma_p$), and post-peak failure stage.

Coal samples exhibit significant anisotropy in the AE evolution at different loading stages.

- (1) Crack closure stage ($0 \sim \sigma_{cc}$): In this stage, pre-existing microcracks and pores within the sample close, resulting in an upward concavity, indicating a gradually increasing stress rate. The cumulative ringing counts for the 0° , 30° , 60° , and 90° samples are 605, 898, 98, and 327, respectively. This is primarily attributed to the gradual compaction of internal pores and cracks within the coal sample under loading, where closure and frictional sliding along crack surfaces and pore walls generate a limited number of AE signals.

Nos.	$\rho/\text{g}\cdot\text{cm}^{-3}$	$v_p/\text{km}\cdot\text{s}^{-1}$	E/GPa	σ_{cc}/MPa	σ_{ci}/MPa	σ_{cd}/MPa	σ_p/MPa
0°-1	1.27	1.38	1.75	4.89	16.95	26.08	34.67
0°-2	1.29	1.42	1.72	3.77	15.01	22.89	28.20
0°-3	1.29	1.46	1.88	4.09	14.97	25.4	33.51
30°-1	1.28	1.48	1.60	4.54	14.57	24.64	33.33
30°-2	1.28	1.27	1.58	4.88	15.16	24.68	31.01
30°-3	1.28	1.38	1.67	3.28	11.58	20.29	26.03
60°-1	1.24	1.81	1.79	2.32	7.41	11.19	14.16
60°-2	1.24	1.78	1.72	1.66	5.83	10.44	14.32
60°-3	1.24	1.85	1.94	2.34	5.6	9.34	13.41
90°-1	1.29	1.93	1.85	3.64	9.67	14.74	20.17
90°-2	1.28	2.00	1.31	2.39	6.34	10.38	13.95
90°-3	1.27	1.70	1.74	2.51	9.29	14.38	17.18

Table 1. Physical and mechanical parameters of different coal samples.

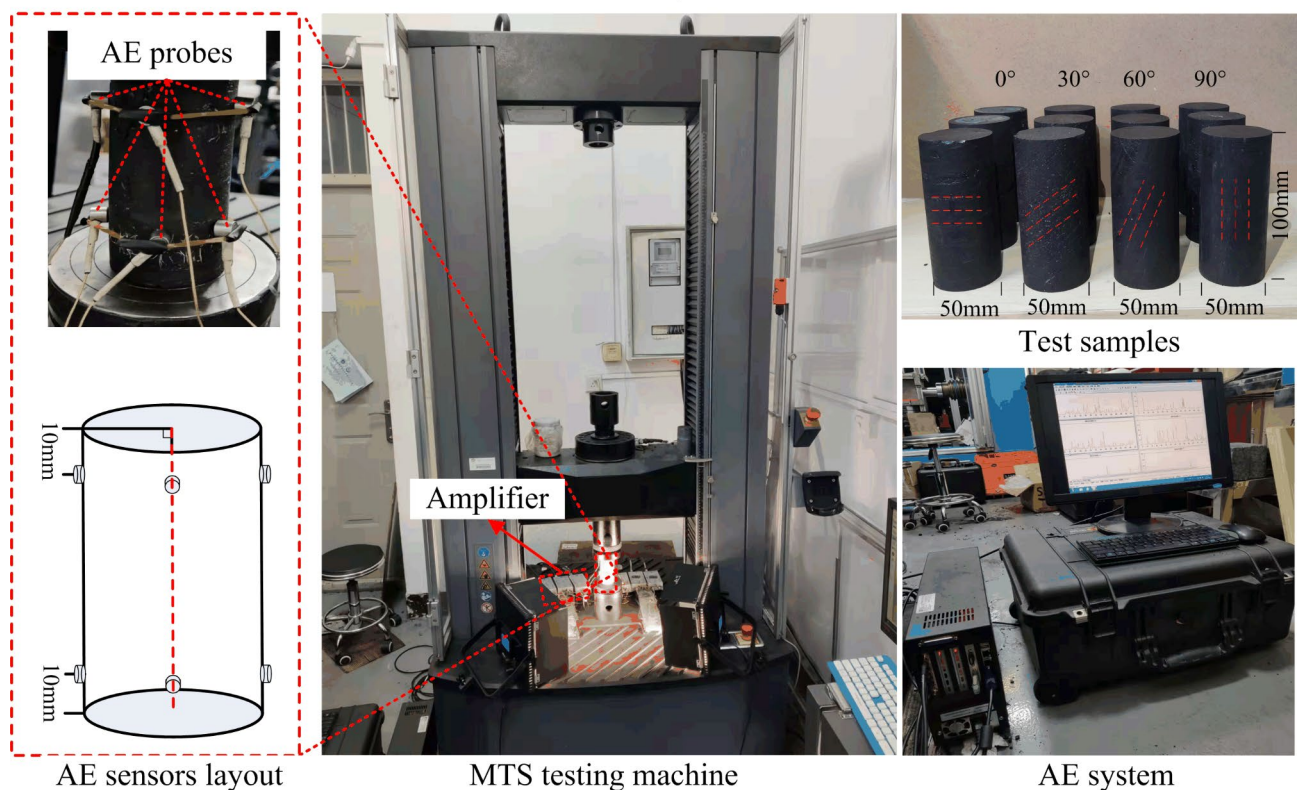


Fig. 2. The diagram of experimental system.

- (2) Linear elastic stage ($\sigma_{cc} \sim \sigma_{ci}$): The stress-strain curve exhibits linear behavior in this stage, with the slope representing the elastic modulus. The average elastic modulus for the samples with different bedding orientations (0°, 30°, 60°, and 90°) are 1.78 GPa, 1.62 GPa, 1.82 GPa, and 1.63 GPa, respectively. The AE activity is relatively low during this stage.
- (3) Stable crack growth stage ($\sigma_{ci} \sim \sigma_{cd}$): With increasing stress, the deformation modulus decreases gradually. Microcracks initiate and propagate within the coal sample. However, through-going macrocracks have not yet formed. The cumulative ringing counts for the coal samples with different bedding orientations in this stage are 11,734, 10,253, 6687, and 1573, respectively.
- (4) Unstable crack growth stage ($\sigma_{cd} \sim \sigma_p$): Microcracks further expand and coalesce, leading to increased internal damage and a further reduction in the load-bearing capacity of the coal. When the bedding orientation is 60°, the stress drop occurs alongside a sharp increase in ringing counts, as shown in Fig. 3(c). Meanwhile, the ringing counts are peak at the end of this stage, with values of 1469, 1449, 2652, and 3292, respectively.
- (5) Post-peak failure stage: Upon exceeding the peak strength of the coal sample, through-going microcracks propagate extensively, leading to a loss of load-bearing capacity. The coal samples with bedding orientations

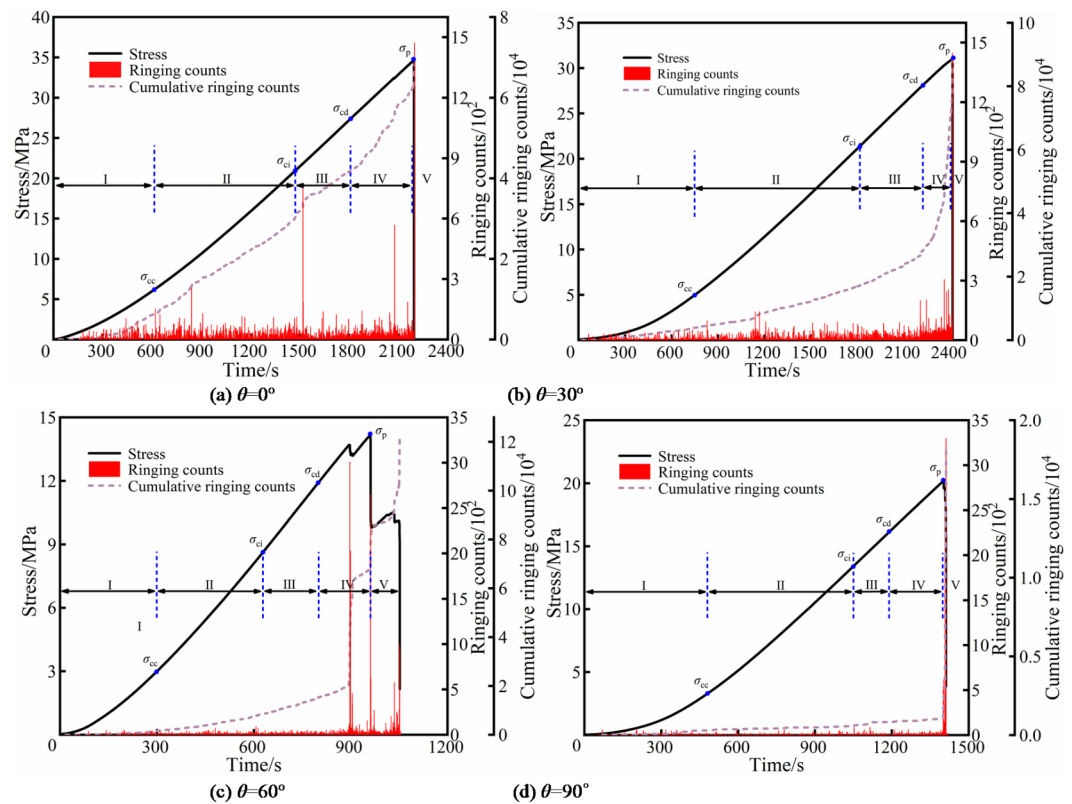


Fig. 3. Evolution of AE counts, accumulated counts and stress with time under uniaxial compression.

of 0° and 30° demonstrate brittle fracture characteristics, exhibiting fewer AE events during the post-peak stage. Conversely, the samples with bedding orientations of 60° and 90° exhibit a more prolonged post-peak failure process, indicative of reduced brittleness. Notably, the sample with bedding orientation of 60° displays a unique stress pattern characterized by a “drop-rise-drop” behavior during the post-peak stage, which is accompanied by a corresponding increase in ringing counts.

Amplitude, a critical parameter reflecting the activity and intensity of the AE signal, can be utilized to characterize the development and evolution of micro-damage in coal samples. Figure 5 illustrates the temporal evolution of amplitude, absolute energy, and stress for coal samples with various bedding orientations under uniaxial compression. The distribution of amplitudes is generally similar, typically ranging from 40 to 100 dB, with the majority concentrated between 40 and 80 dB. However, the amplitude distribution varies significantly across different stages. During the compaction stage, amplitudes range from 40 to 80 dB, predominantly concentrated between 40 and 65 dB, with absolute energy below 10^5 aJ. In the linear elastic stage, fewer AE events exhibit amplitudes greater than 80 dB and absolute energy less than 10^6 aJ, with most amplitudes remaining within 40 to 80 dB. As the samples transition into the unstable crack growth stage, events with amplitudes exceeding 90 dB become more frequent, and absolute energy surpasses 10^7 aJ. Effective AE signals are not detected during the failure stage for the coal samples at 0° and 30° due to the failure. In contrast, when the bedding orientation is 60° , a significant number of AE signals are still recorded, attributed to the stepwise stress drops observed in the post-peak stage. Consequently, the frequent occurrence of high-amplitude and high-energy AE signals serves as an indicator of impending coal failure.

Figure 6 presents the AE amplitude distribution for the coal samples with different bedding orientations under uniaxial compression. The proportion of different amplitude ranges is generally consistent across all bedding orientations. Low amplitudes (40–60 dB) constitute the highest proportion (approximately 80%), while the proportion of higher amplitudes (> 60 dB) is lower and decrease with increasing amplitude. Curve fitting revealed an exponential relationship between the proportion of events within each amplitude range and the amplitude for all bedding orientations.

Evolution characteristics of microcracks

The AE characteristics provide a qualitative indication of progressive rock failure and are linked to the failure mode. In this study, the AE source location calibration was performed. Figure 7 compares the failure morphology of the samples with the corresponding AE event locations. Macroscopic cracks in the samples with bedding orientations of 0° and 30° are oriented perpendicular to the bedding planes. In contrast, the microcracks of the coal sample at 60° propagate along the bedding planes, while those in the sample with bedding orientation of 90° are oriented parallel to the bedding planes. Furthermore, the AE source locations indicate that events with higher

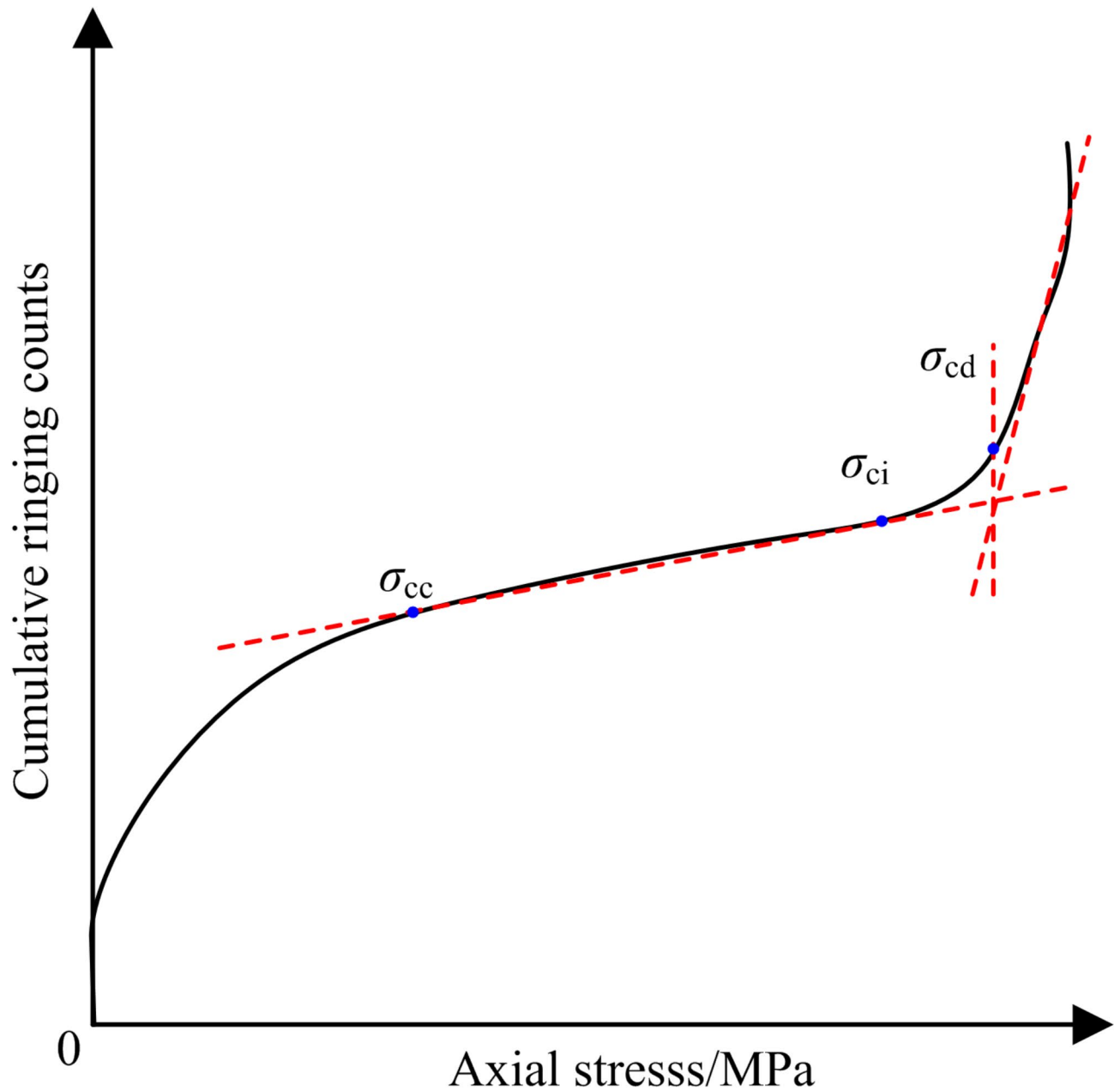


Fig. 4. Calculation method of stress characteristic point.

amplitudes are predominantly concentrated near the main fracture zones. This study analyzed the evolution of the AE parameters AF and RA to further investigate development of microcracks during the deformation and failure process. AF and RA, key parameters in AE signal analysis, serve as valuable indicators for identifying rock failure modes and monitoring damage evolution. Tensile stresses typically induce tensile cracks, characterized by AE signals with high AF and low RA values. Conversely, shear cracks are generally associated with low AF and high RA values, as illustrated in Fig. 8. The AF and RA values were calculated as follows:

$$RA = \frac{\text{rise time}}{\text{amplitude}} \quad (1)$$

$$AF = \frac{\text{ringing counts}}{\text{duration}} \quad (2)$$

A threshold method was employed to classify crack types. Specifically, when the ratio $k = AF/RA$ exceeds a predefined threshold, it is classified as a tensile crack; otherwise, it is classified as a shear crack. It should be noted that the threshold value, k , is typically determined empirically and varies depending on the material being tested. For instance, Ohno et al.²⁹ used a threshold of $k = 80$ to classify crack types during the failure of concrete

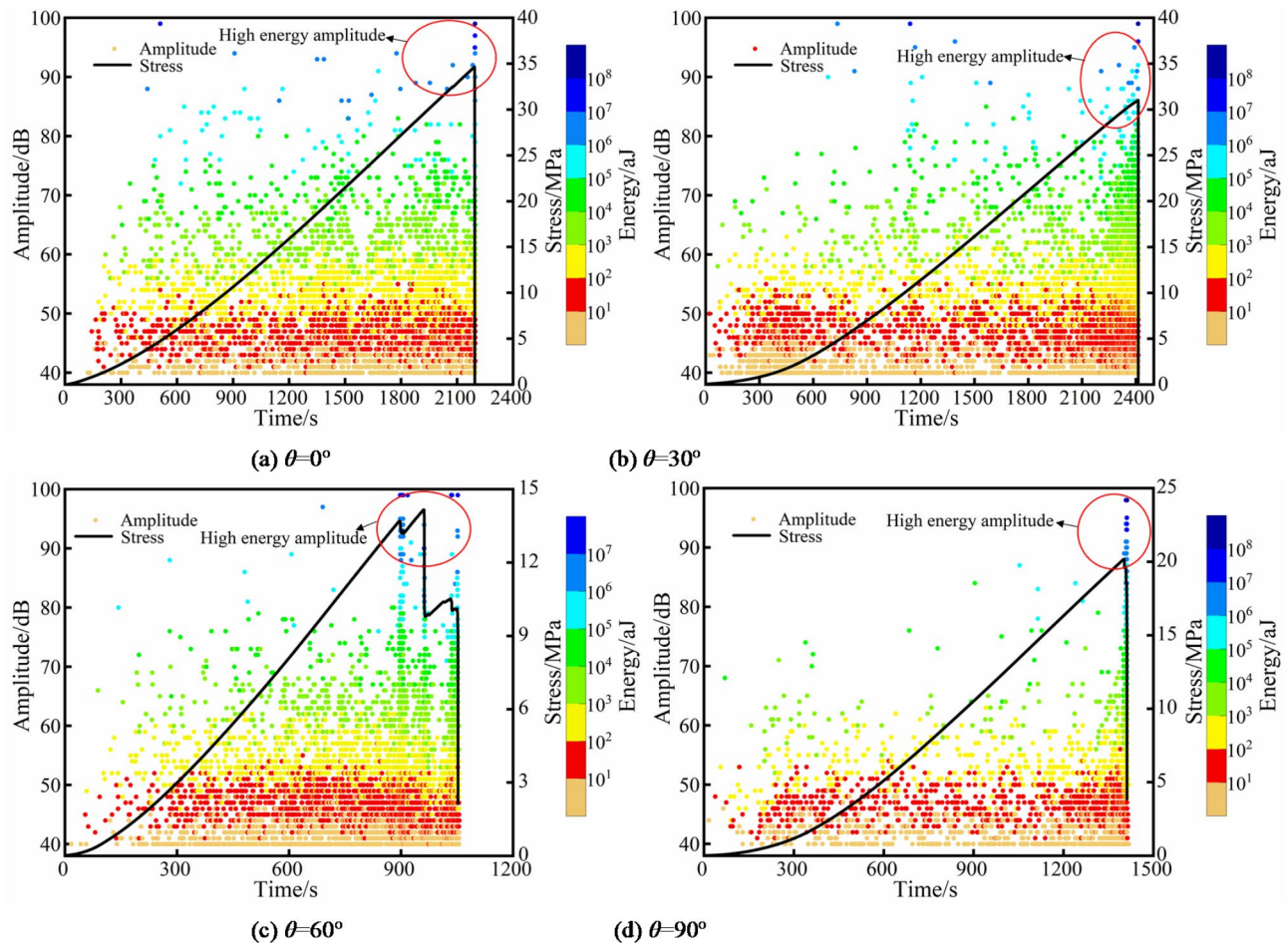


Fig. 5. Amplitude-absolute energy and stress evolution with time under uniaxial compression.

samples. Similarly, Yu et al.³⁰ employed a threshold of $k = 30$ for crack-type classification in concrete. Ding et al.³¹ compared the evolution of tensile and shear cracks in sandstone using thresholds of $k = 100$ and $k = 500$. Han et al.³² and Gao et al.²⁸ analyzed the proportions of shear and tensile cracks in coal samples at different loading stages using k values of 0.5, 1.0, 2.0, and 3.0, suggesting that a k value of 2 minimized the error. According to Gao et al.²⁸ and Han et al.³², unprocessed coal samples exhibited uniaxial compressive strength of 18.26 MPa and 25.9 MPa, respectively, with corresponding elastic modulus of 2.97 GPa and 3.78 GPa. With the increase in strength among different types of coal samples, the threshold of $k = 2$ could be used to classify the shear and tensile failure during the failure process. In this study, the uniaxial compressive strength of coal samples with different bedding orientations ranges from 13.41 MPa to 34.67 MPa, and the elastic modulus ranges from 1.31 GPa to 1.94 GPa. Therefore, the threshold of $k = 2$ is also selected as the reference line to define different types of fracture signals.

Figure 9 illustrates the temporal variations in AF/RA values and the number of microcracks for coal samples with different bedding orientations. Different colors are utilized to represent the scatter plots of AF/RA values corresponding to each stage of stress evolution. The total numbers of microcracks observed during the loading process for coal samples with bedding orientations of 0° , 30° , 60° , and 90° were 4913, 6573, 6780, and 3652, respectively. As shown in Fig. 10, when the bedding orientation is 0° , the proportion of tensile cracks reaches 86.59%, indicating that failure is predominantly tensile. With an increase in bedding orientation from 0° to 60° , the proportion of tensile cracks decreases to 14.10%, while the proportion of shear cracks increases from 13.41 to 85.90%. This shift suggests that as the bedding orientation increases, the failure mode transitions from tensile to shear. When the bedding orientation increases to 90° , the proportion of tensile cracks rises again to 82.50%, while the proportion of shear cracks decreases to 17.50%, indicating that the 90° sample also exhibits predominantly tensile failure. To further investigate the crack evolution characteristics of coal samples with different bedding orientations, the proportions of tensile and shear cracks at various loading stages were statistically analyzed, as summarized in Table 2. It can be observed that as stress increases, both the numbers of shear and tensile cracks exhibit an upward trend. Microcracks development within the coal samples is most pronounced during the σ_{cd} - σ_p and post-peak failure stages, accounting for approximately 70% of the entire loading process. Additionally, the proportion of cracks in the post-peak stage is higher for the 60° and 90° samples compared to the 0° and 30°

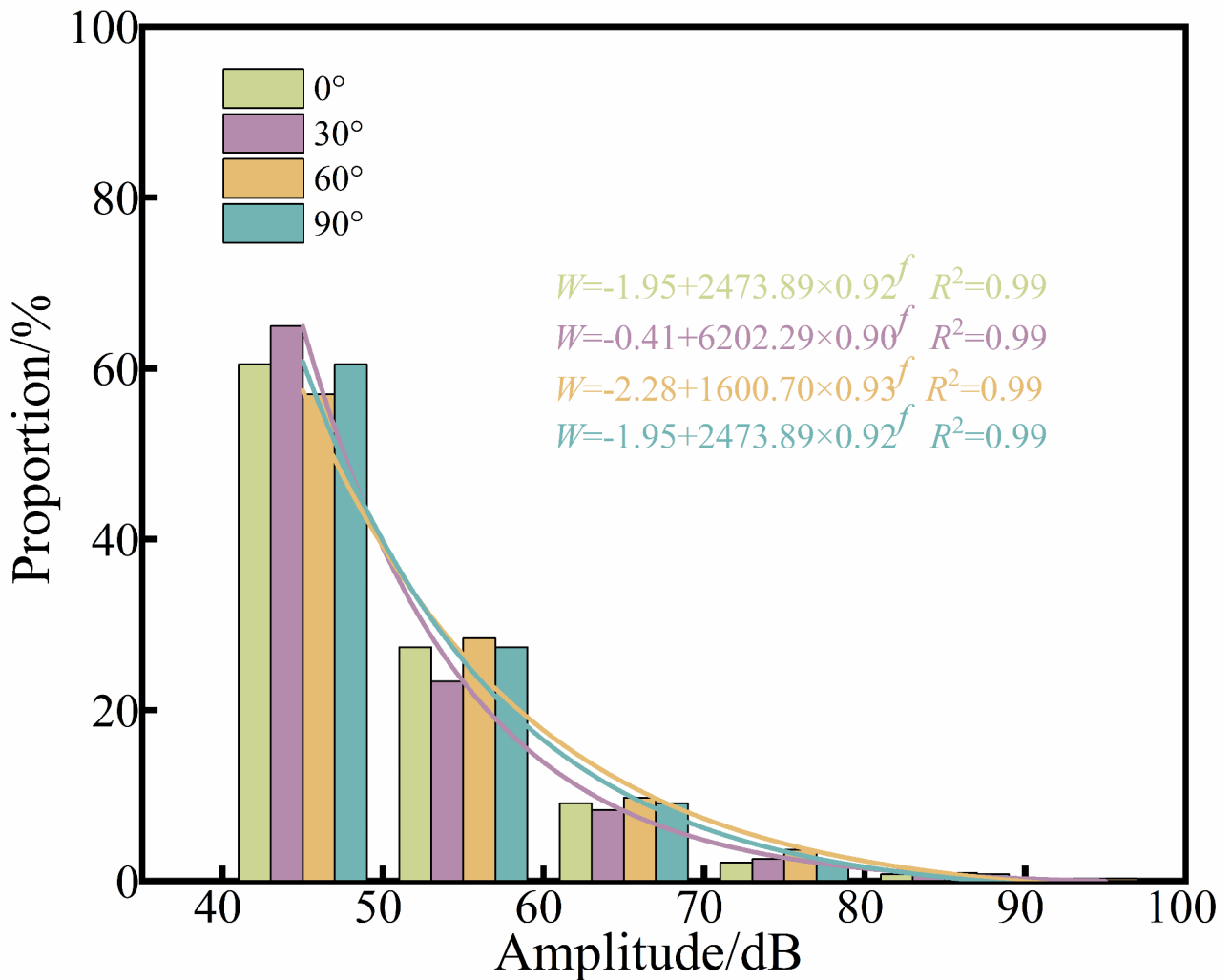


Fig. 6. Distribution of amplitude for coal samples under uniaxial compression.

samples, further indicating that the latter two samples experience a shorter post-peak failure stage and exhibit distinct brittle behavior.

Evolution of b -values

The b -value characterizes the relationship between the magnitude and frequency of AE events generated during coal sample failure, providing valuable insights into the evolution of microcracks within rock during deformation and failure. A decrease in the b -value indicates the growth and coalescence of larger cracks, while an increase suggests the development of smaller cracks. The steps for calculating the b -value are as follows:

(1) Collect the arrival time (t) and amplitude (A_{db}) of the AE signals recorded by the monitoring system, and calculate the AE event magnitude (M):

$$M = A_{db}/20 \quad (3)$$

(2) A suitable sampling window is selected for b -value analysis. Previous studies have demonstrated that while the choice of sampling window and step size can influence the calculated b -values at different time points, the overall trend of b -value evolution over time remains generally consistent. In this study, a sampling window of 1000 AE events was employed.

(3) To calculate the b -value, the event magnitude range is divided into width intervals $\Delta M = 0.5$. The number of AE events (N) falling within each magnitude interval is then counted. Finally, the b -value for that group of events is determined by performing a linear fit based on Eq. (4) according to the Gutenberg-Richter rules³³:

$$\lg N = a - bM \quad (4)$$

(4) The b -value for each group of 1000 events was calculated using the method described in step (3). By analyzing these values, the temporal evolution of the b -value was characterized.

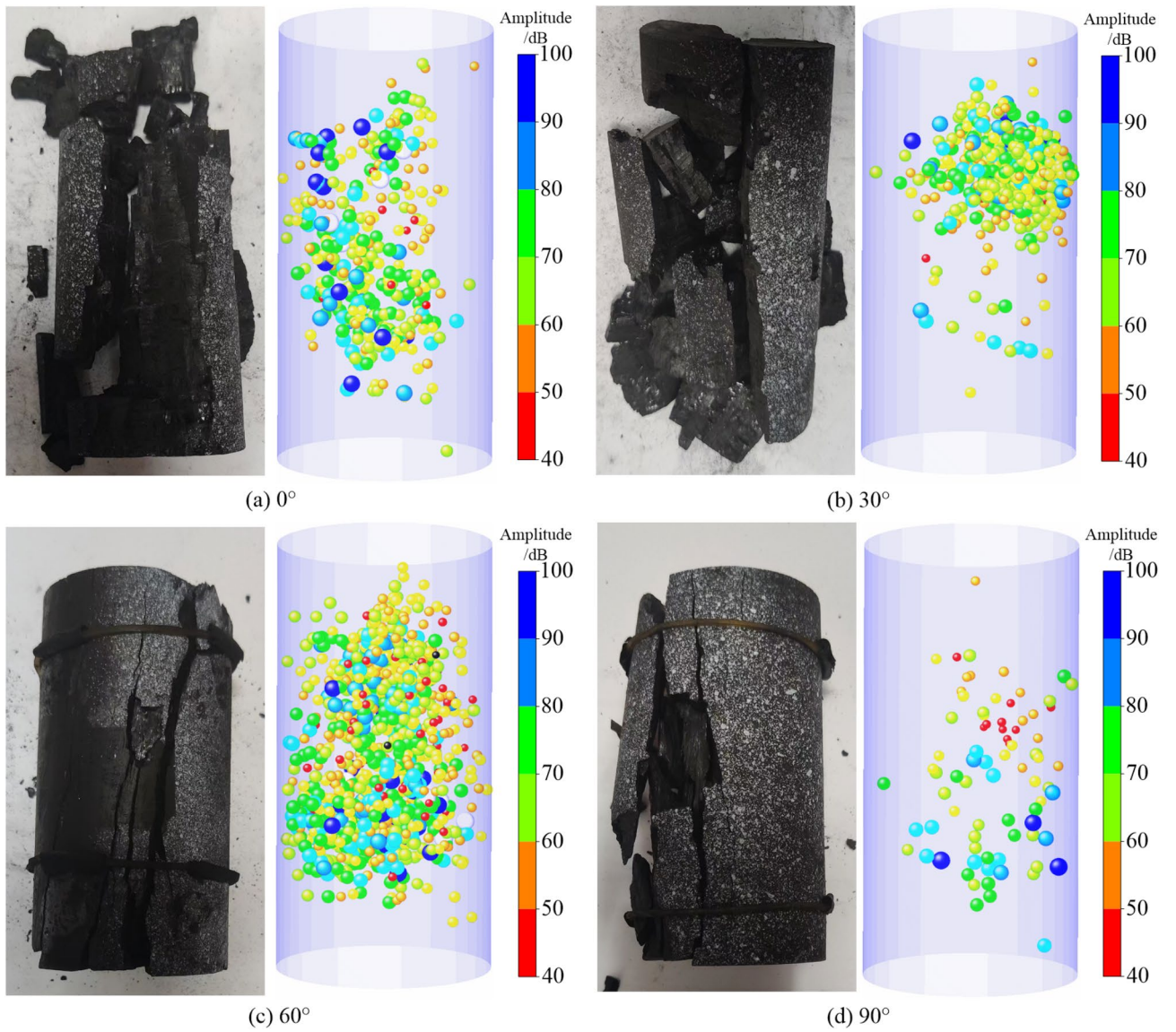


Fig. 7. AE source location and failure pattern for coal samples with different bedding plane orientations. The 3D images were created by OriginPro 2025b Beta, <https://www.originlab.com/>.

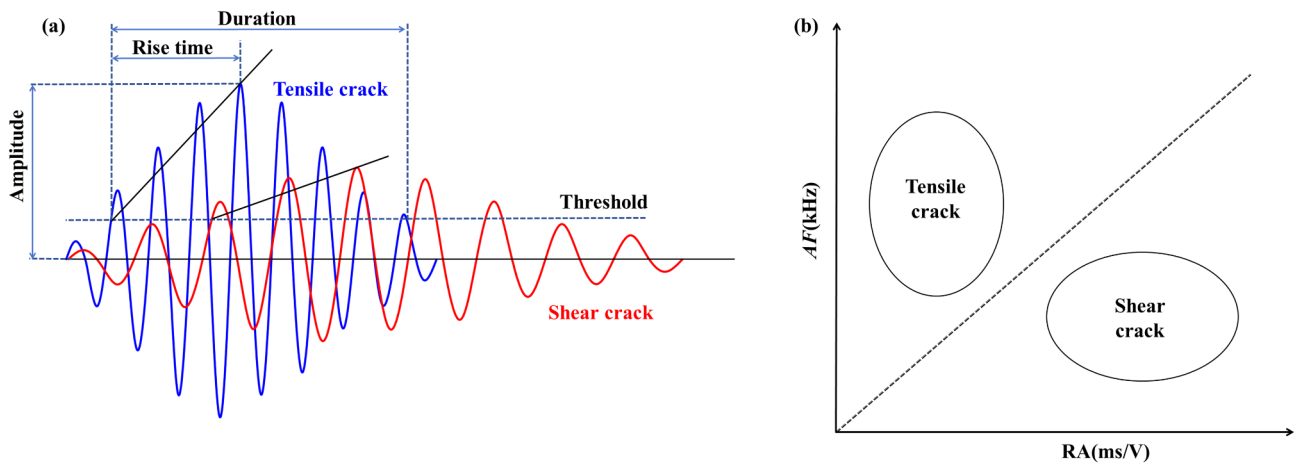


Fig. 8. Schematic diagram of AF and RA value calculation²⁸.

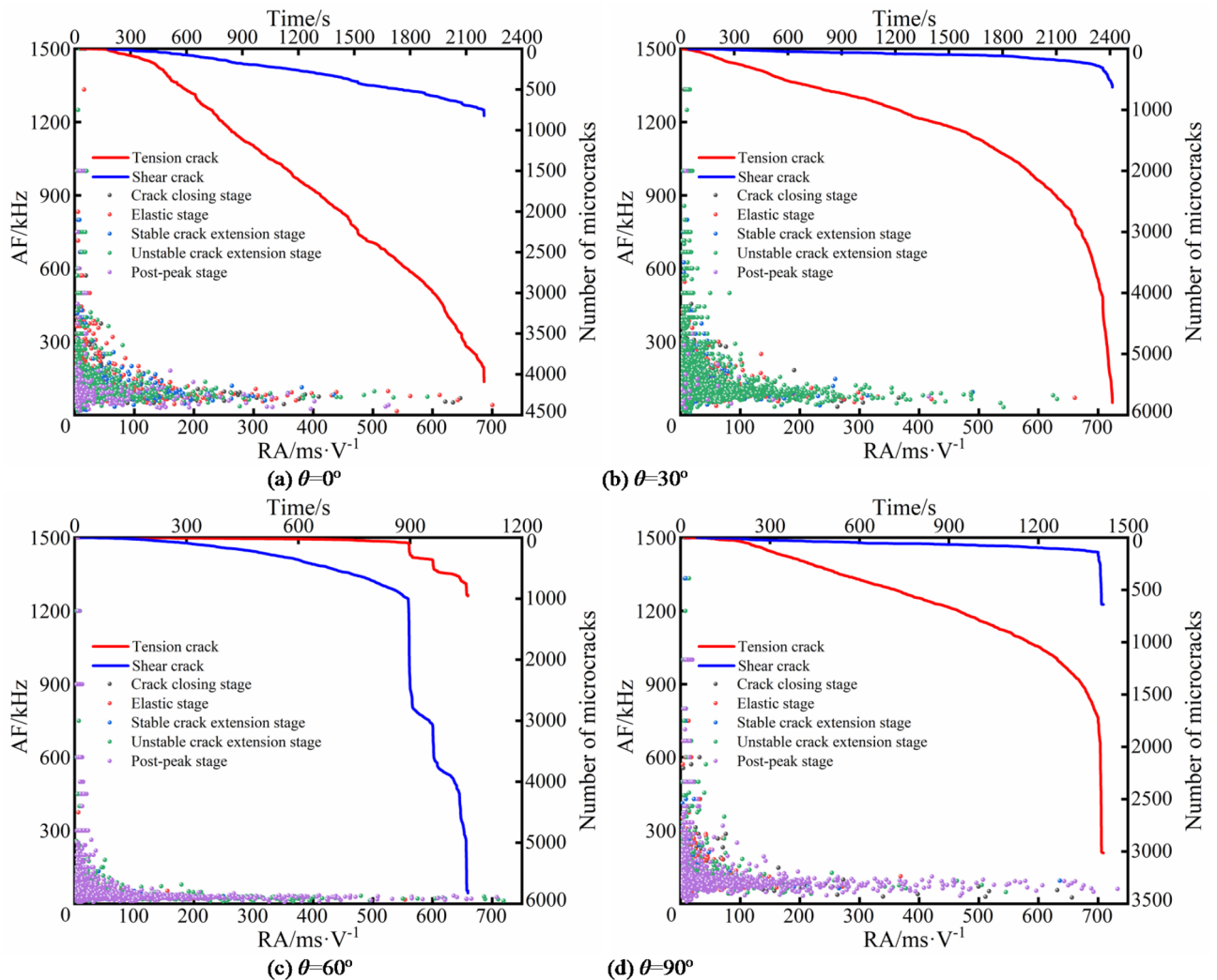


Fig. 9. Evolution of AF/RA values and the number of microcracks over time in coal samples.

Figure 11 illustrates the fluctuation characteristics of the b -value for coal samples with different bedding orientations. The temporal evolution of the b -value was generally consistent across all samples, ranging from 0.6 to 1.3. During the crack closure stage, the b -value exhibits fluctuations of varying magnitudes. This is primarily attributed to the compaction of pre-existing microcracks within the coal sample and the dislocation between particles during crack closure, leading to further crack development. Variations in the distribution of pre-existing microcracks among samples with different bedding orientations resulted in differing degrees of b -value fluctuation. During the linear elastic stage, microcracks initiation and propagation are stabilized, accompanied by a slight increase in irreversible deformation, resulting in smaller b -value fluctuations. Then, during the unstable crack growth stage, microcracks develop rapidly and coalesce. Consequently, the stored energy within the coal sample is released abruptly, accompanied by a surge in high-energy AE events, leading to a significant decrease in the b -value. Dong et al.³⁴ proposed using the minimum b -value observed during the unstable crack growth stage as a precursor for predicting rock failure. The precursor time points for the samples with bedding orientations of 0°, 30°, 60°, and 90° are determined to be 2030.94 s, 2330.47 s, 905.44 s, and 1269.34 s, respectively, with corresponding stress levels at the precursor points of $0.91\sigma_c$, $0.93\sigma_c$, $0.92\sigma_c$, and $0.88\sigma_c$. The average stress level at the precursor point is $0.91\sigma_c$.

Damage evolution of bedded coal

Deformation and failure in coal and rock masses result from the accumulation and subsequent release of energy. Fundamentally, this process involves the initiation, propagation, and eventual coalescence of internal microcracks under external loading, accompanied by the emission of acoustic signals. A damage variable, D , can be defined based on the cumulative ringing counts as follows³⁵:

$$D = \frac{C_d}{C_s} \quad (5)$$

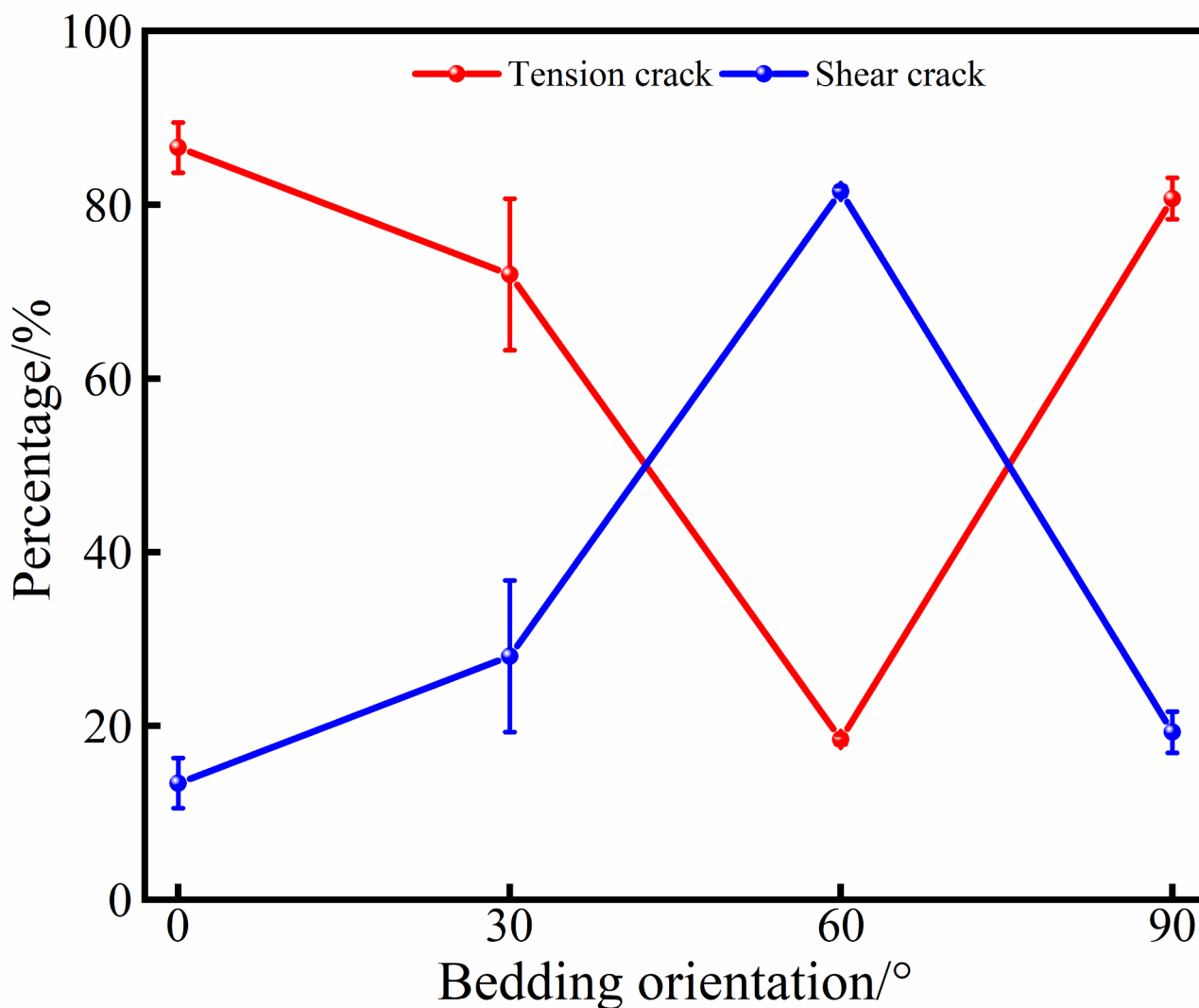


Fig. 10. The percentage of tension and shear microcracks in coal samples at different bedding orientations.

Nos.	0- σ_{cc} stage		σ_{cc} - σ_{ci} stage		σ_{ci} - σ_{cd} stage		σ_{cd} - σ_p stage		After peak stage		Total	
	Tension/%	Shear/%	Tension/%	Shear/%	Tension/%	Shear/%	Tension/%	Shear/%	Tension/%	Shear/%	Tension/%	Shear/%
0°-1	10.71	1.61	31.59	5.98	13.60	2.97	23.67	4.66	3.70	1.51	83.27	16.73
0°-2	3.82	0.60	18.40	3.43	21.00	3.11	39.68	4.17	5.65	2.41	88.55	11.45
0°-3	11.37	1.28	29.99	3.40	15.95	1.89	24.20	5.38	6.46	2.23	87.96	12.04
30°-1	3.91	2.26	6.75	1.84	5.44	3.95	50.88	17.71	7.02	3.45	74.00	26.00
30°-2	6.70	2.40	9.13	1.95	12.11	4.25	51.40	11.80	0.16	0.09	79.50	20.50
30°-3	4.64	4.95	4.18	5.00	13.68	7.76	39.67	19.70	0.28	0.14	62.44	37.56
60°-1	0.43	1.00	1.02	4.10	0.97	3.79	10.64	29.52	17.91	30.62	18.42	81.58
60°-2	0.32	1.54	0.84	3.45	1.48	10.26	10.78	50.86	4.47	15.99	17.89	82.11
60°-3	0.31	1.74	0.48	6.06	1.05	9.28	7.89	44.87	9.30	19.02	19.02	80.98
90°-1	7.91	1.04	15.09	1.07	5.26	0.44	19.85	2.08	34.39	12.87	82.50	17.50
90°-2	9.24	3.06	3.75	0.83	6.74	0.87	49.69	3.06	12.23	10.53	81.65	18.35
90°-3	1.79	0.41	5.39	0.83	10.30	1.77	50.23	14.36	10.31	4.61	78.02	21.98

Table 2. The percentage of tension and shear microcracks at various stages during loading.

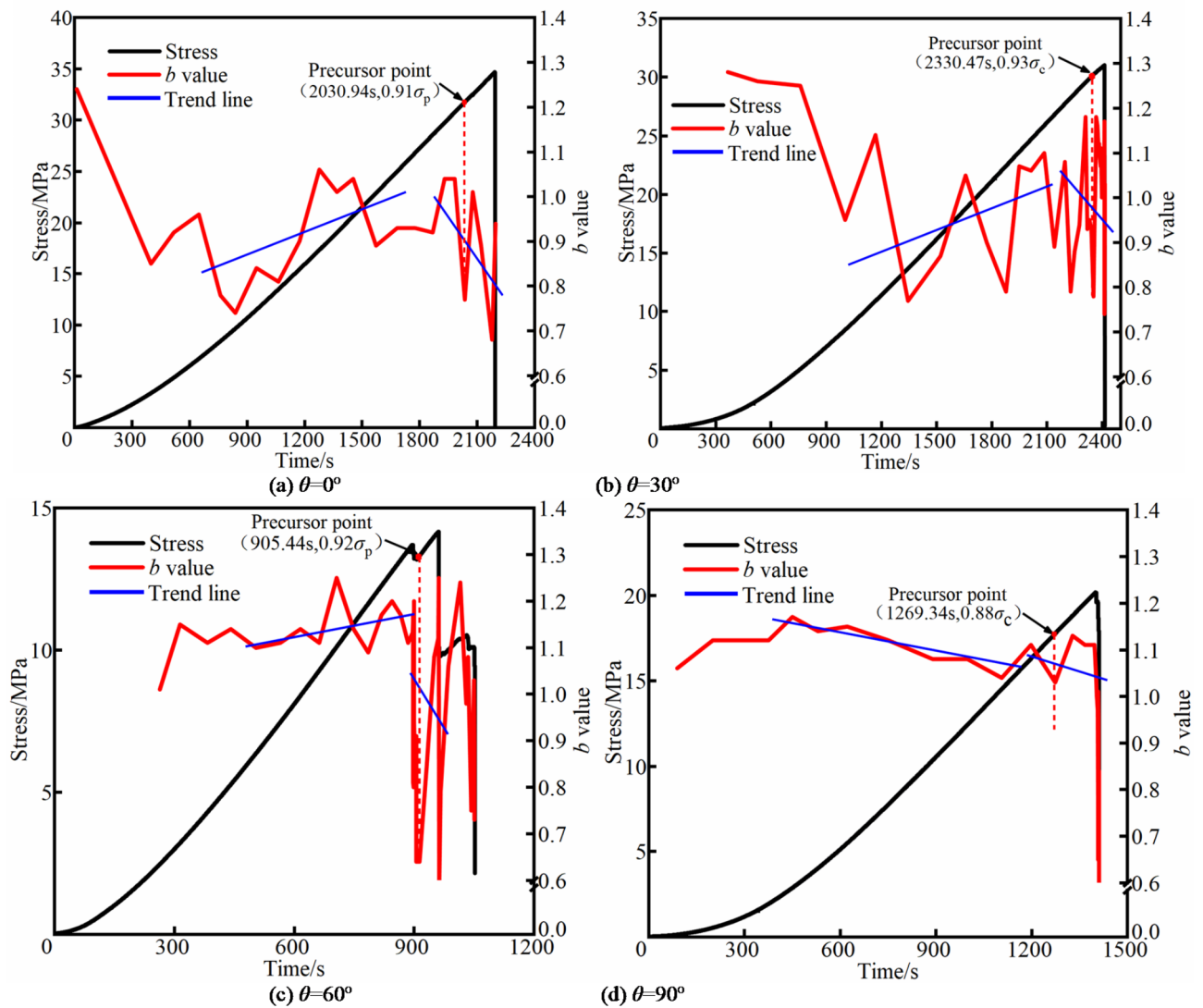


Fig. 11. Evolution of the b -value at different bedding coal samples under uniaxial compression.

Where C_d represents the cumulative ringing counts at a given time prior to failure, and C_s represents the cumulative ringing count at complete failure.

The damage variable for coal samples with different bedding orientations was calculated based on the experimental results, and the axial strain was normalized. The evolution of the damage variable during the deformation and failure process for coal samples with different bedding orientations is shown in Fig. 12. The damage evolution in coal samples under uniaxial compression can be divided into three stages as strain increases: the initial damage stage (I), the damage development stage (II), and the damage acceleration stage (III). In the initial damage stage, the damage variable (D) approaches 0. This is because the coal sample undergoes compaction, with internal cracks gradually closing, resulting in negligible internal damage. During the damage development stage, the damage variable (D) increases gradually, exhibiting an approximately linear trend. The sample transitions into the plastic deformation stage. As the external load increases, microcracks initiate and propagate within the sample, leading to a continuous accumulation of internal damage. Upon entering the damage acceleration stage, the damage variable (D) increases rapidly. Internal cracks propagate and coalesce, resulting in a loss of load-bearing capacity and macroscopic failure of the coal sample.

During the damage development stage, the samples with different bedding orientations exhibit distinct differences in behavior. The damage variable curve for the bedding orientation of 0° exhibits a stepwise increase, indicating that the loading direction is perpendicular to the bedding planes. According to Jager's criterion, the bedding planes have no influence on crack propagation and failure within the matrix. Microcracks gradually expand and coalesce within the coal matrix, as illustrated in Fig. 13(a). The AE activity is significant, and internal damage within the sample continuously increases, leading to a stepwise increase in the damage variable. The sample with the bedding orientation of 30° exhibits tensile-shear failure, as Fig. 13(b) illustrates. The AE activity is weaker when microcracks propagate along the bedding planes but intensifies when microcracks through the bedding planes. Consequently, the damage accumulation during deformation is lower for the sample with

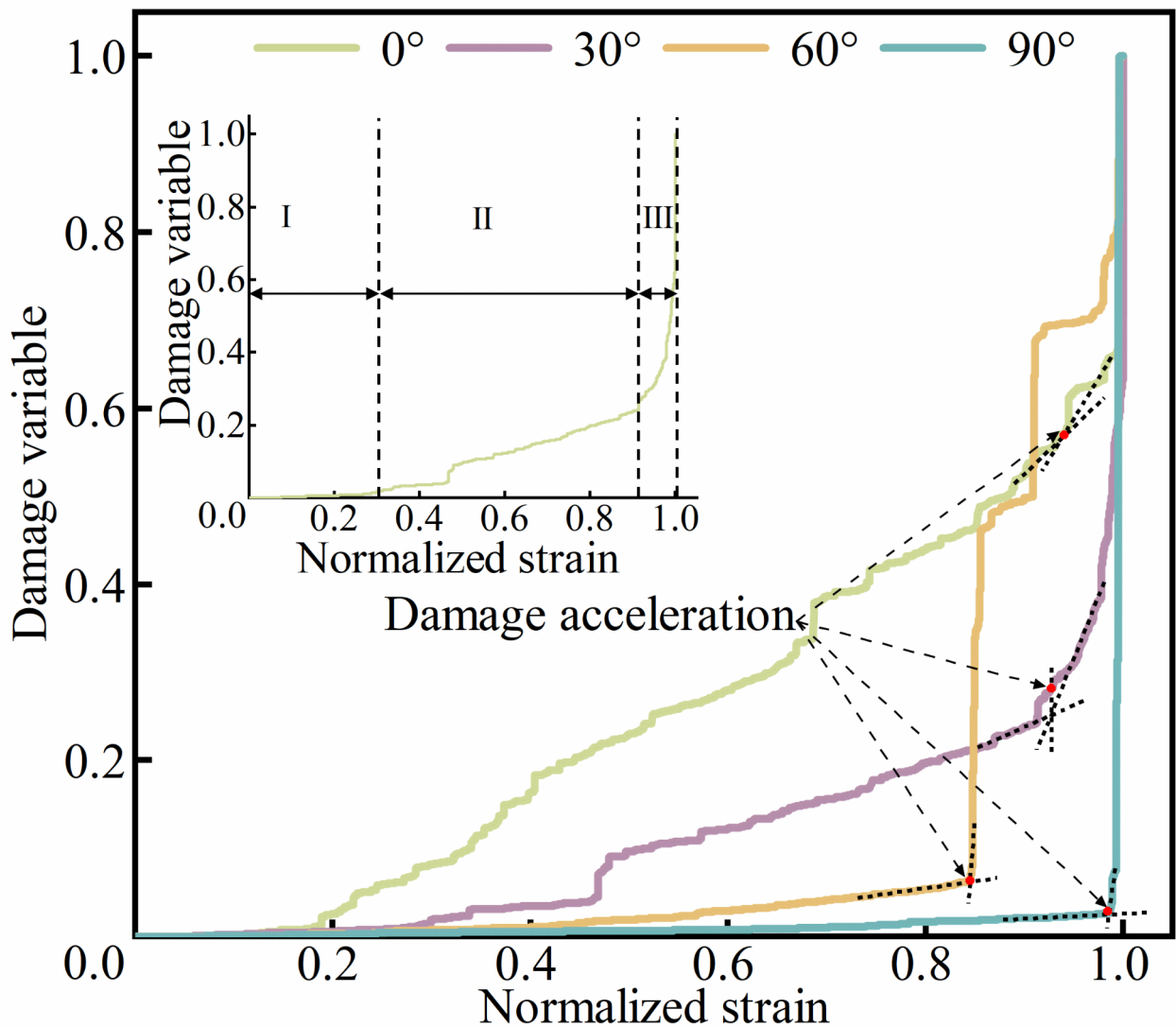


Fig. 12. Damage evolution curve under uniaxial compression.

a bedding orientation of 30° . The samples with bedding orientations of 60° and 90° exhibit a “stable-sudden increase” pattern in the damage evolution. For the sample at 60° , the damage variable remains below 0.05 between 0 and $0.82\varepsilon_p$. Microcracks initiation and propagation occur predominantly along the bedding planes, suggesting minimal microcrack development within the sample during this period. Then, it experiences a sudden increase beyond $0.82\varepsilon_p$. Similarly, the sample with a bedding orientation of 90° exhibits a damage variable below 0.02 between 0 and $0.99\varepsilon_p$, followed by a sudden increase near the peak stress. This is attributed to the fact that the sample with a bedding orientation of 90° fails predominantly in tension. Microcracks propagate along the bedding planes, leading to continuous spalling from the sample surface, as illustrated in Fig. 13(d). Due to coal’s significantly lower tensile strength compared to its compressive strength, the sample is susceptible to tensile failure. Frictional effects between the bedding planes are negligible, resulting in fewer AE events. Consequently, the damage variable curve remains nearly horizontal initially. Damage accumulation accelerates as the sample approaches failure.

Prior to the failure of the coal sample, the internal damage evolution exhibits a pronounced acceleration effect. This acceleration signifies the rapid propagation and accumulation of microcracks within the coal sample, resulting in a significant increase in the degree of damage. As evidenced by the damage evolution curve, this phenomenon is characterized by a sudden steepening of the slope, indicating a marked increase in the rate of damage progression. To quantitatively describe this feature, this study defines the intersection point of the slopes of the damage evolution curves before the peak stress as the “damage acceleration point”, as shown in Fig. 12. This point delineates the transition from the stable damage accumulation phase to the instability failure phase and holds important physical significance. The sequence of damage acceleration for the coal samples at different bedding orientations is $60^\circ < 30^\circ < 0^\circ < 90^\circ$. This ordering primarily results from the fact that tensile failure requires significantly more energy compared to shear failure. Tensile failure necessitates overcoming

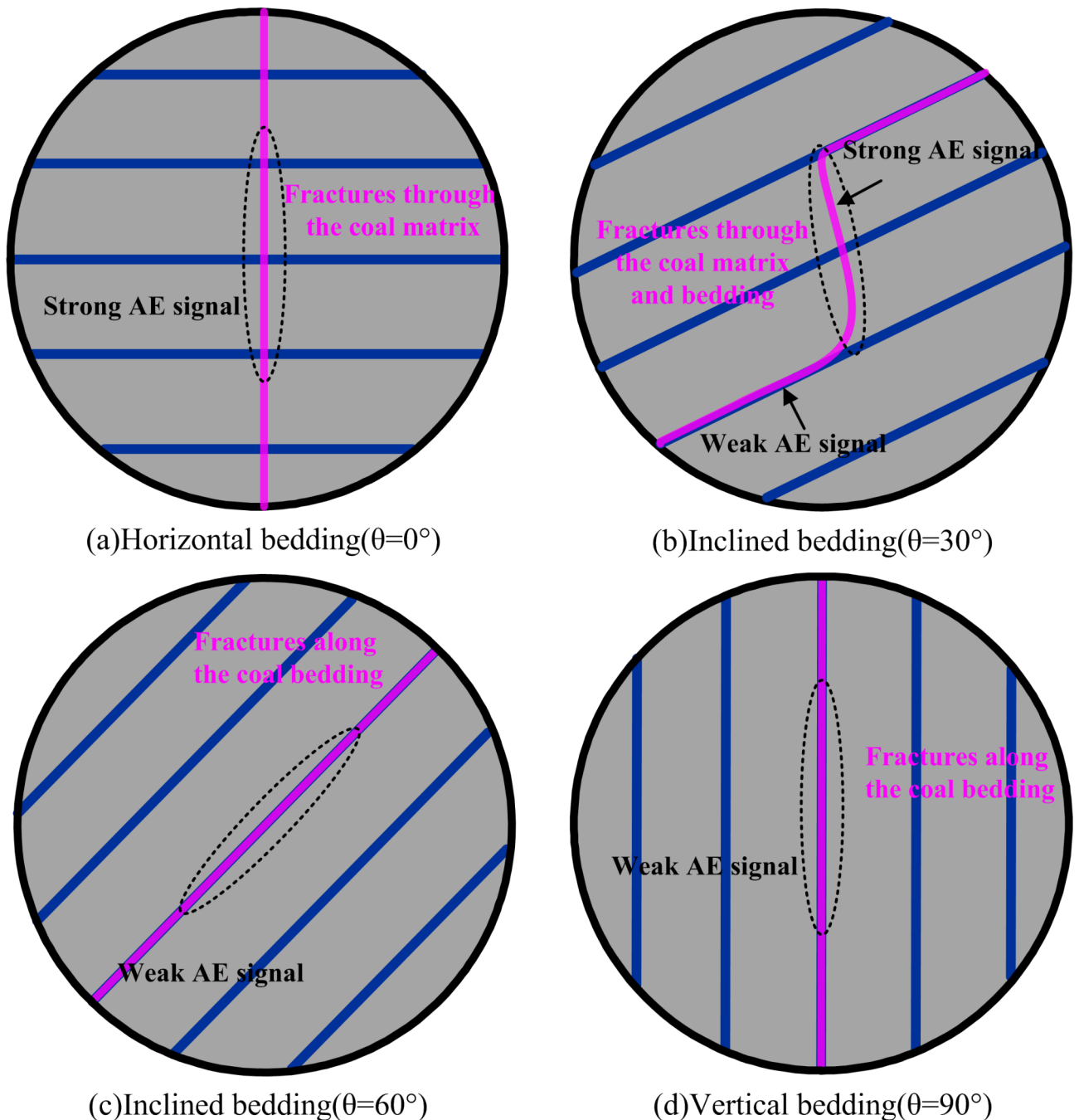


Fig. 13. Failure mechanisms of coal samples with varying bedding orientations.

internal cohesion and friction, as well as withstanding concentrated and uneven stresses, leading to microcracks propagation and greater energy release. In contrast, shear failure only needs to overcome the strength of the bedding plane, which requires less energy for specimen failure, as illustrated in Fig. 13(c). Consequently, the coal sample at 60° exhibits the most pronounced acceleration phenomenon, while the 90° sample experiences the latest onset of acceleration damage.

Precursor response characteristics of AE signals

Different parameters represent distinct physical phenomena and often exhibit unique characteristics during deformation and failure. However, these parameters typically have different units and scales, making direct comparison challenging. This complicates the visual assessment of the sequence of precursor changes across different parameters and their interrelationships. Therefore, this study employs a linear normalization technique to process the AE parameters obtained during the deformation and failure of coal samples, as illustrated in Fig. 14. This transform converts each parameter into a dimensionless value, eliminating unit and scale dependencies.

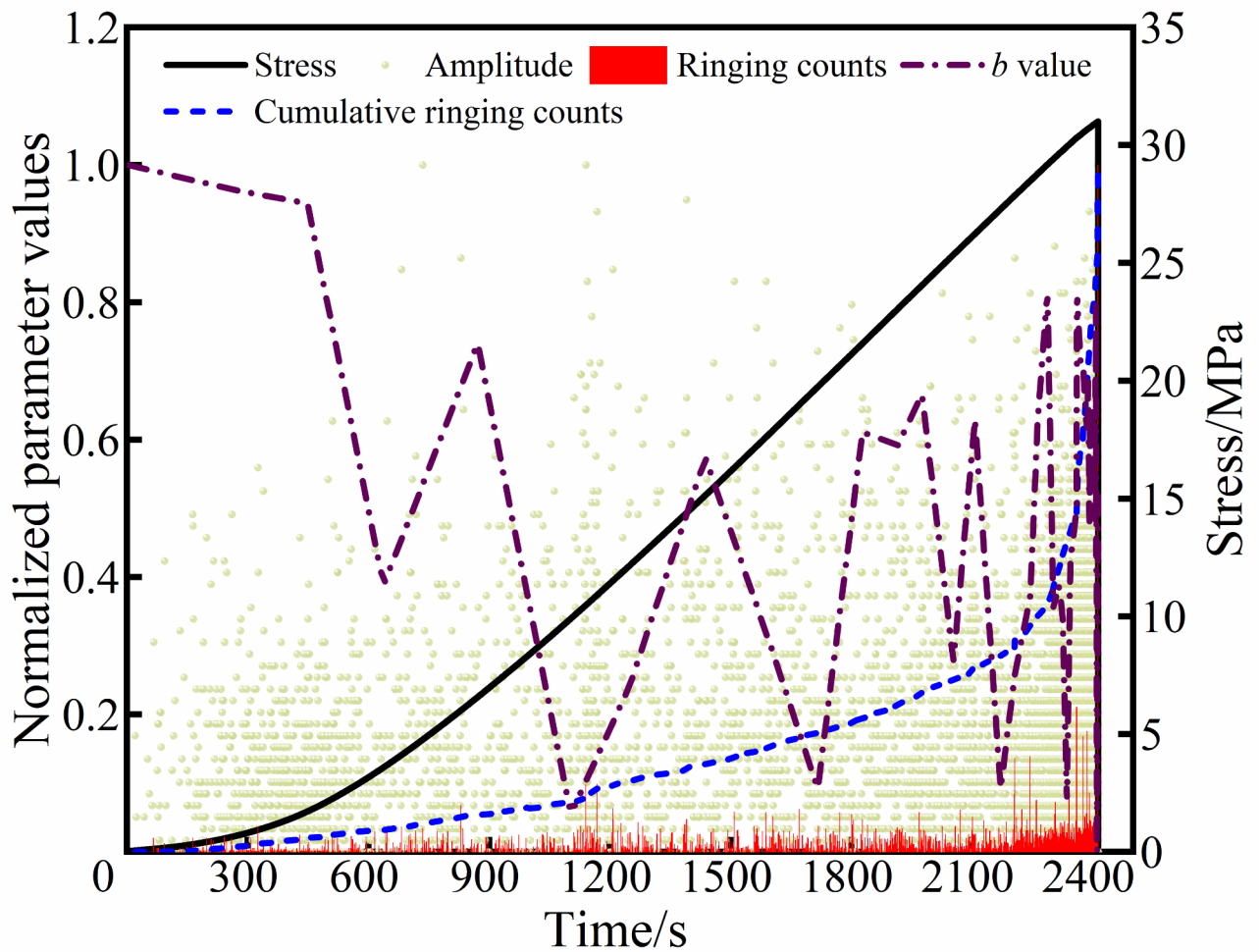


Fig. 14. Normalized curves of AE parameters during deformation and failure (30° bedding orientation sample as an example).

Importantly, this normalization procedure preserves the underlying physical meaning of each parameter and does not alter the relative relationships between data points. As the coal sample approaches failure, various AE parameters exhibit abrupt changes, either increasing or decreasing sharply. These distinct changes can serve as precursory indicators for predicting coal sample failure. The characteristic precursory changes observed in each parameter are described below: (1) Amplitude: prior to coal failure, a sustained increase in high-amplitude AE events is observed. (2) Ringing counts: during the initial loading stages, ringing counts remain relatively low. However, a sudden increase is observed as the sample approaches failure. (3) Cumulative ringing counts: during the initial loading stages, the cumulative ringing count exhibits a stepwise increase corresponding to microcrack development. A sharp increase in cumulative ringing counts is observed prior to failure. (4) The b -value: initially, the b -value fluctuates around a relatively high value, but it drops rapidly to a minimum as the sample enters the imminent failure stage.

$$\alpha = \frac{t_{\max} - t_i}{t_{\max}} \quad (6)$$

Where t_i is the time corresponding to the precursor point, s; t_{\max} is the time corresponding to the peak stress, s.

The precursor response coefficients for four AE parameters were calculated and compared, as shown in Table 3. The precursor response coefficients, in descending order, are: the b -value > cumulative ringing count > amplitude > ringing counts. The AE b -value exhibits the earliest precursor timing, indicating its superior sensitivity and predictive capability for dynamic disasters. Jiang et al.^{36,37} conducted uniaxial compression tests on backfill materials, elucidating the crack development mechanism within samples through b -value analysis, thereby providing a robust theoretical foundation for backfill applications. Furthermore, Jiang et al.^{38,39} performed uniaxial compression tests on coal and coal-rock composites under cyclic water immersion conditions, analyzing the AE and damage characteristics during the failure processes. This research offers critical theoretical support for the stability analysis of underground mine reservoirs. Due to the sudden nature and multifaceted influencing factors associated with dynamic disasters in mining operations, relying on a single

Nos.	Precursor response coefficient			
	Amplitude	Ringing counts	Cumulative ringing counts	b value
0°-1	0.025	0.011	0.052	0.074
0°-2	0.018	0.019	0.063	0.042
0°-3	0.012	0.025	0.049	0.059
Mean value	0.018	0.019	0.055	0.058
30°-1	0.006	0.021	0.019	0.061
30°-2	0.023	0.008	0.024	0.034
30°-3	0.017	0.008	0.042	0.060
Mean value	0.015	0.012	0.028	0.052
60°-1	0.032	0.008	0.057	0.058
60°-2	0.014	0.016	0.044	0.051
60°-3	0.018	0.006	0.048	0.049
Mean value	0.021	0.010	0.049	0.053
90°-1	0.006	0.002	0.001	0.117
90°-2	0.019	0.011	0.037	0.069
90°-3	0.008	0.006	0.027	0.044
Mean value	0.011	0.006	0.022	0.077

Table 3. Precursory response coefficients of AE parameters for different bedding coal samples. To quantitatively evaluate the precursory response capability of each parameter, a precursor response coefficient, denoted as α , is introduced. A larger α value indicates an earlier precursor response time and, consequently, a more effective precursor. The calculation formula is as follows:

parameter has significant limitations and may not be sufficient for effectively identifying the occurrence of such disasters in practical applications. By normalizing the parameters to a common scale, a comprehensive analysis of the interrelationships and precursory response capabilities of multiple parameters can significantly enhance the effectiveness and accuracy of coal failure prediction.

Energy evolution of coal during deformation and failure

Strain energy calculation

The deformation of coal under external loading involves the accumulation and release of energy, as shown in Fig. 15. The presence of bedding planes leads to variations in the failure characteristics of coal samples, resulting in distinct differences in their energy accumulation and dissipation patterns. Assuming an isolated and closed system, where external forces induce damage in coal, the principle of energy conservation dictates the following relationship among these energy components:

$$U = U^e + U^d \quad (7)$$

Where U represents the total strain energy, J/cm^3 ; U^e represents the elastic strain energy, J/cm^3 ; and U^d represents the dissipated energy, J/cm^3 .

As the uniaxial compression test involves work done only in the axial direction, the various strain energy components can be determined by integrating the area under the stress-strain curve. Furthermore, based on previous studies, the unloading modulus (E_u) is generally similar to the elastic modulus (E), allowing the latter to be used as an approximation in these calculations. Therefore, the total strain energy (U), elastic strain energy (U^e) and dissipated energy (U^d) can be calculated using the following equations:

$$U = \int_0^\varepsilon \sigma d\varepsilon \quad (8)$$

$$U^e = \frac{1}{2E} \sigma^2 \quad (9)$$

$$U^d = \int_0^\varepsilon \sigma d\varepsilon - \frac{1}{2E} \sigma^2 \quad (10)$$

Figure 16 illustrates the temporal evolution of energy for coal samples with varying bedding orientations. The strain energy evolution exhibits similar patterns across different bedding orientations. With increasing loading time, the total strain energy (U) generally shows an upward concave growth trend. Initially, it increases non-linearly at an accelerating rate. Subsequently, it transitions to an approximately linear increase with a stable rate. The evolution of elastic strain energy (U^e) closely follows that of the total strain energy (U). This is primarily because the elastic strain energy is directly related to the elastic modulus of the rock. Upon reaching the peak stress, the elastic strain energy (U^e) also peaks, indicating the maximum storage capacity for elastic strain energy within the sample. During the post-peak failure stage, the elastic strain energy (U^e) decreases rapidly as the

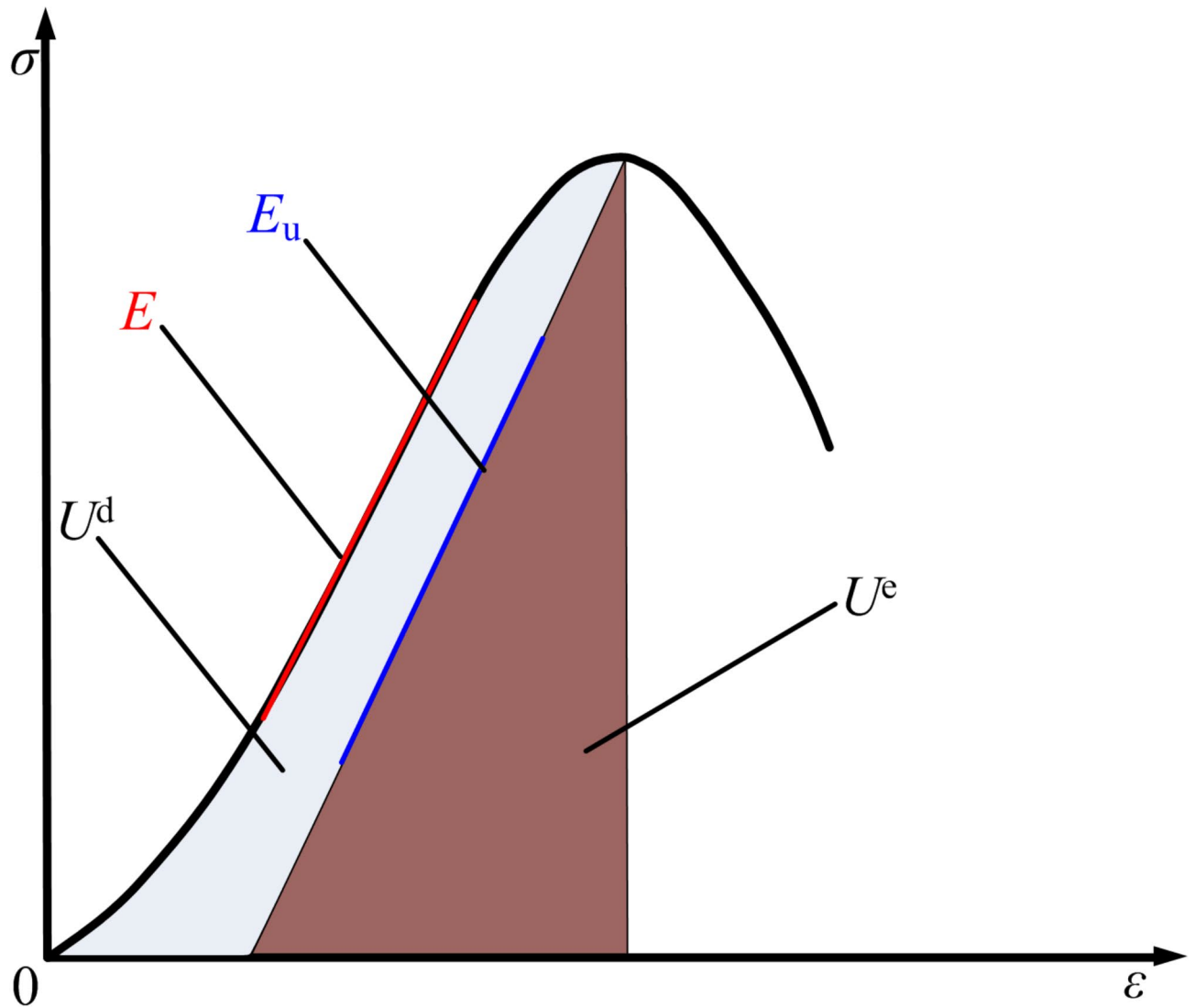


Fig. 15. Energy evolution diagram.

sample undergoes macroscopic failure. This storage capacity limit dictates whether the sample will experience irreversible macroscopic damage. The dissipated energy (U^d) remains at a relatively low level prior to the peak stress but surges during the post-peak failure stage. Localized damage within the coal sample corresponds to abrupt increases in the dissipated energy, as shown in Fig. 16(c).

Anisotropic characteristics of energy evolution

Table 4 presents the energy statistics for coal samples with different bedding orientations at various characteristic stress points. The average values were calculated, and the variation of each strain energy component with bedding orientation were illustrated in Fig. 17. As shown in Table 4; Fig. 17, at the crack closure stress point (σ_{cc}), the U , U^e , and U^d for the sample at 0° are 0.00911, 0.00524, and 0.00387 J/cm³, respectively. As the bedding orientation increases to 60° , the U , U^e , and U^d decrease to 0.00246, 0.00158, and 0.00089 J/cm³, respectively. At a bedding orientation of 90° , the U , U^e , and U^d increase to 0.00464, 0.00278, and 0.00186 J/cm³, respectively. At the crack initiation stress point (σ_{ci}), the U , U^e , and U^d for the 0° sample increase to 0.07627, 0.06394, and 0.01233 J/cm³, respectively. With increasing bedding orientation, all energies reach their minimum values at 60° , specifically 0.01329, 0.01053, and 0.00276 J/cm³. Similarly, at the damage stress point (σ_{cd}), each energy exhibits a V-shaped trend, reaching maximum values at 0° of 0.17498, 0.15916, and 0.01582 J/cm³, respectively, and minimum values at 60° of 0.03055, 0.02820, and 0.00235 J/cm³, respectively. At the crack initiation stress point (σ_{ci}) and the damage stress point (σ_{cd}), the dissipated energy shows low sensitivity to the bedding orientation, exhibiting a similar trend, suggesting that energy accumulation dominated during these stages. Conversely, the total strain energy and elastic strain energy show higher sensitivity to the bedding orientation.

Furthermore, the evolution of strain energy at the peak stress, concerning the bedding orientation, is generally consistent with that observed at the damage stress point. The sample with bedding orientation of 0° exhibited the highest total strain energy at peak stress, reaching 0.29348 J/cm³, indicating that it required the

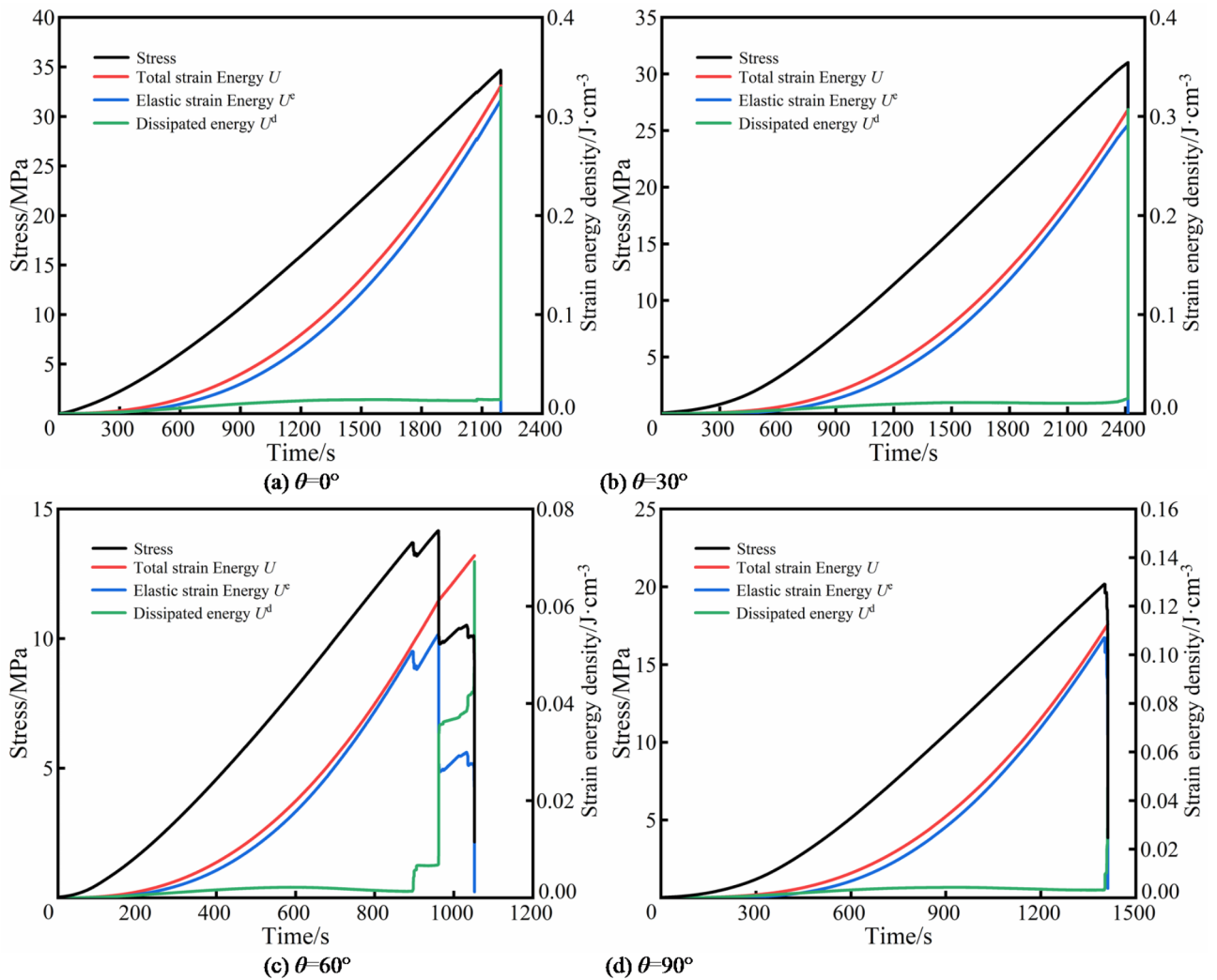


Fig. 16. Evolution of strain energy in coal samples with different bedding orientations.

Nos.	σ_{cc}			σ_{ci}			σ_{cd}			σ_p		
	U	U ^e	U ^d	U	U ^e	U ^d	U	U ^e	U ^d	U	U ^e	U ^d
0°-1	0.01095	0.00657	0.00438	0.08930	0.07582	0.01348	0.19191	0.17826	0.01365	0.33052	0.31627	0.01425
0°-2	0.00695	0.00487	0.00208	0.07178	0.06028	0.01150	0.16096	0.13888	0.02208	0.26376	0.20935	0.05442
0°-3	0.00943	0.00429	0.00514	0.06774	0.05573	0.01200	0.17020	0.16034	0.00986	0.28615	0.28069	0.00546
30°-1	0.00969	0.00653	0.00316	0.07266	0.06508	0.00758	0.19208	0.18534	0.00674	0.35112	0.33658	0.01454
30°-2	0.01285	0.00779	0.00505	0.08088	0.07035	0.01053	0.19671	0.18618	0.01053	0.30707	0.29148	0.01559
30°-3	0.00643	0.00428	0.00214	0.04341	0.03966	0.00375	0.12540	0.12004	0.00536	0.21053	0.19930	0.01123
60°-1	0.00225	0.00161	0.00064	0.01693	0.01479	0.00214	0.03558	0.03376	0.00182	0.06109	0.05421	0.00688
60°-2	0.00249	0.00177	0.00072	0.01281	0.00897	0.00383	0.03277	0.02906	0.00371	0.06575	0.05394	0.01181
60°-3	0.00265	0.00135	0.00131	0.01015	0.00783	0.00232	0.02329	0.02178	0.00152	0.05674	0.04499	0.01175
90°-1	0.00600	0.00343	0.00257	0.02898	0.02469	0.00429	0.06122	0.05711	0.00411	0.11038	0.10709	0.00328
90°-2	0.00476	0.00320	0.00156	0.01963	0.01049	0.00914	0.04149	0.02822	0.01327	0.06686	0.05118	0.01568
90°-3	0.00318	0.00172	0.00146	0.02669	0.02265	0.00404	0.05955	0.05469	0.00486	0.09570	0.07763	0.01807

Table 4. Strain energy statistics of different stress characteristic points.

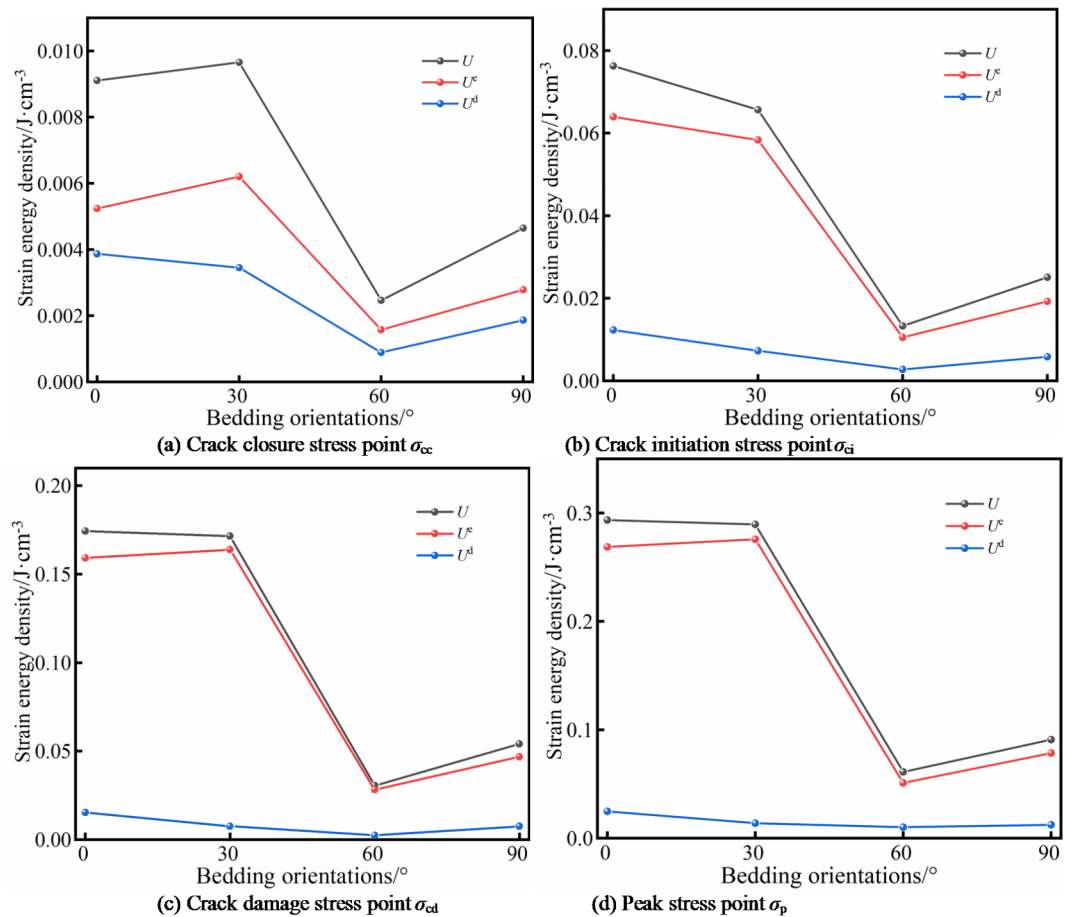


Fig. 17. Evolution of strain energy at different stress characteristic points with different bedding orientations.

most energy to fail and was the most resistant to failure. In contrast, the sample with a 60° bedding orientation required the least total strain energy for failure, 0.06119 J/cm³, suggesting it was the most susceptible to failure. This is primarily because the sample with bedding orientation of 60° failed predominantly through shear along the bedding planes, leading to lower energy dissipation. Conversely, the sample with bedding orientation of 0° failed in tension, with cracks propagating across the bedding planes, resulting in higher strength and more significant energy accumulation before reaching the peak stress. This demonstrates a strong correlation between the macroscopic failure mode and the strain energy required for failure, further highlighting the anisotropic nature of strain energy and failure mode about bedding orientation.

Figure 18 illustrates the evolution of the ratio of strain energy to total strain energy for different bedding orientations. The average ratios of elastic strain energy at the crack closure, crack initiation, crack damage, and peak stress points are 2.39%, 20.09%, 52.05%, and 89.17%, respectively. At the crack closure stress point (σ_{cc}), the ratios of elastic strain energy to total strain energy are closely clustered around the average value for all bedding orientations, indicating low sensitivity of the elastic strain energy ratio to bedding orientation. At the crack damage stress point (σ_{cd}), the sample with bedding orientation of 60° exhibits the lowest elastic strain energy ratio, at 46.05%. This suggests that a smaller amount of stored elastic strain energy is sufficient to initiate accelerated damage in this sample. As supported by Fig. 12, this observation provides further evidence from an energy perspective that the sample with bedding orientation of 60° experiences the earliest onset of damage acceleration. At the peak stress point (σ_p), the elastic strain energy ratios are more widely distributed. The sample bedding orientation of 30° had the highest value, reaching 95.24%, while the 60° bedding orientation sample has a significantly lower percentage of 83.42%, a difference of 11.82%. This further demonstrates that the sensitivity of the elastic strain energy ratio to bedding orientations increases with the increasing stress.

To further characterize the anisotropy of the strain energy components, the degree of strain energy anisotropy was calculated at different characteristic stress points. Figure 19 shows that at the crack closure stress point (σ_{cc}), the degree of anisotropy for total strain energy, elastic strain energy, and dissipated energy are 3.92, 3.94, and 4.36, respectively. At the damage stress point (σ_{cd}), the degree of anisotropy for total strain energy, elastic strain energy, and dissipated energy increases to 5.71, 5.81, and 6.47, respectively. Additionally, as stress increases, the degree of anisotropy for total strain energy, elastic strain energy, and dissipated energy initially increase and then decrease.

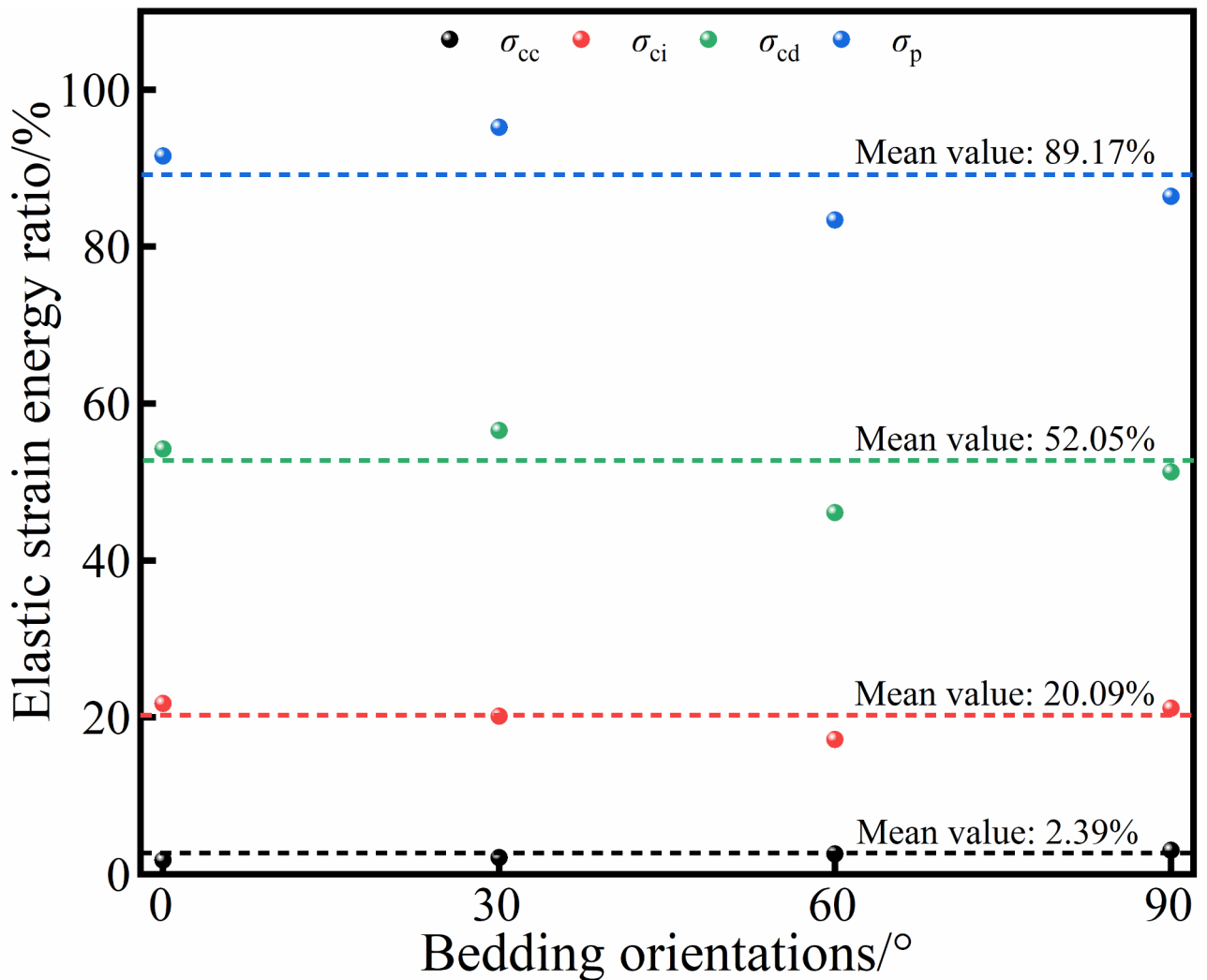


Fig. 18. Elastic energy ratio of coal samples with different bedding orientations.

Conclusions

This study aims to analyze the anisotropic characteristics of AE and energy evolution in bedded coal under uniaxial compression. The main conclusions are as follows:

- (1) Bedding planes significantly influence the AE activity of coal during deformation and failure. As the bedding orientation increases, the cumulative ringing counts exhibit pronounced anisotropic characteristics in different loading stages. The amplitude is concentrated in the range of 40~80 dB throughout loading process, with high-energy amplitude signals generated during the unstable crack extension stage. In contrast, the sample with bedding orientation of 60° exhibit lower energy amplitude is compared to the samples with other bedding orientations.
- (2) When the bedding orientation is 0°, the tensile cracks account for 86.59% of all microcracks, indicating that failure is predominantly due to tensile stress. As the bedding orientation increases to 60°, the proportion of tensile cracks decreases to 14.10%, while shear cracks increase to 85.90%, suggesting that failure is primarily shear-induced. At a bedding orientation of 90°, the proportion of tensile cracks rises again to 82.50%, indicating that failure returns to being mainly tensile. The development of microcracks within the coal sample is most active during the unstable crack extension stage and the post-peak failure stage, accounting for approximately 70% of the entire loading process.
- (3) The AE parameters show different precursor characteristics before the imminent failure of the coal sample: amplitude, ringing counts, and cumulative ringing counts show sudden increases, while the precursor characteristic of the b -value exhibits a sudden drop. The precursor response capabilities of the AE parameters are also different. The order of the precursor response coefficient for coal sample failure is the b -value > cumulative ringing count > amplitude > ringing counts.
- (4) The total strain energy (U), elastic strain energy (U^e) and dissipated energy (U^d) of the coal samples show a trend of initially decreasing and then increasing at each characteristic stress point, reaching the minimum value when the bedding orientation is 60°. With the increase stress, the anisotropy degree of total strain

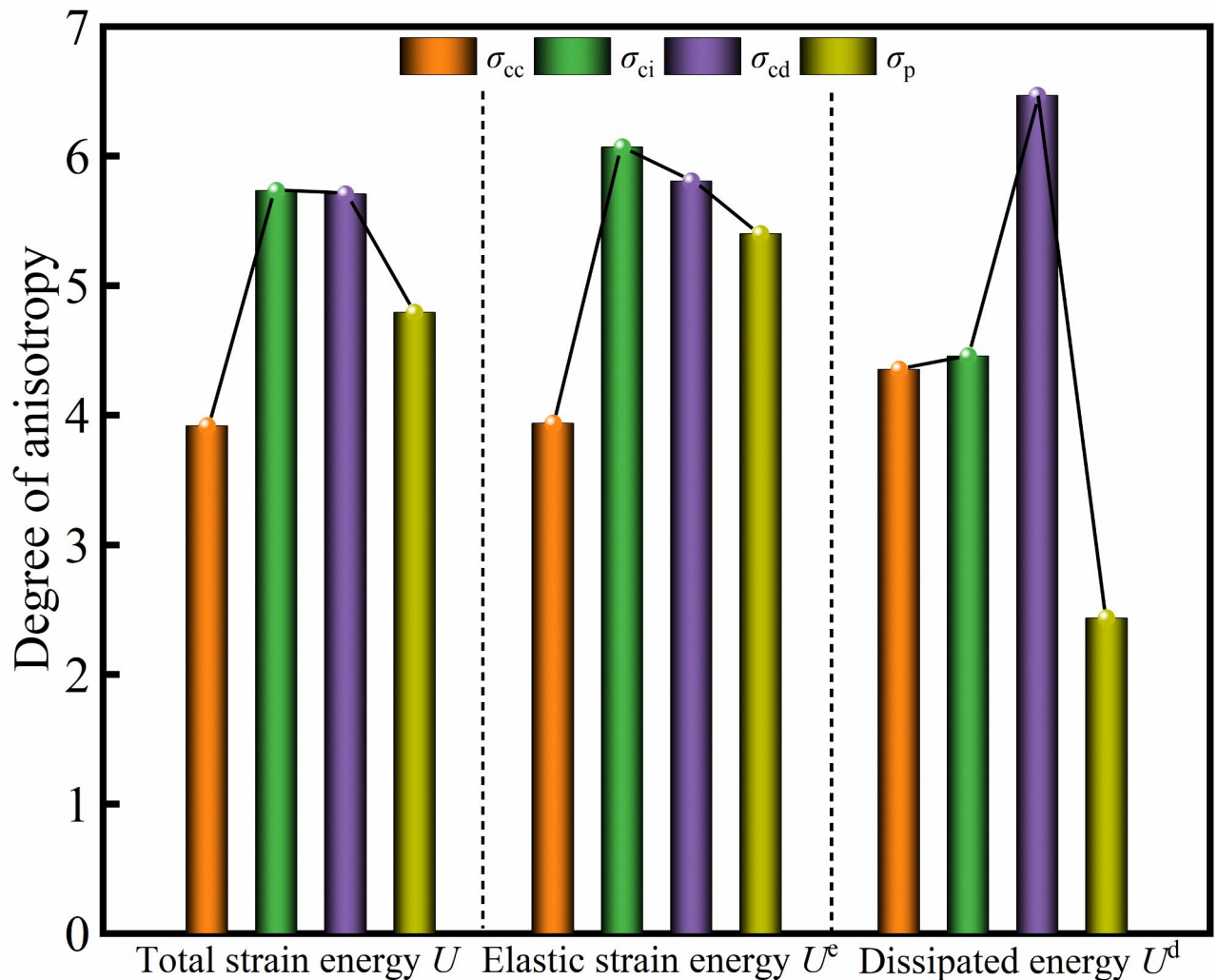


Fig. 19. Anisotropy degree of strain energy at different stress characteristic points.

energy (U), elastic strain energy (U^e), and dissipated energy (U^d) shows a V-shaped variation trend. The degree of anisotropy is the highest at the crack initiation stress point (σ_{ci}) and the lowest at the crack closure stress point.

Data availability

The datasets used during the current study available from the corresponding author on reasonable request.

Received: 10 January 2025; Accepted: 3 April 2025

Published online: 12 April 2025

References

1. Wang, J. et al. Study on the controller factors associated with roof falling and ribs spalling in deep mine with great mining height and compound roof. *Eng. Fail. Anal.* **129**, 105723 (2021).
2. Liu, S., Yang, K. & Tang, C. A. Mechanism and Integrated Control of Rib Spalling: Roof Collapse-Support Instability Hazard Chains in Steeply Dipping Soft Coal Seams. *Adv. Mater. Sci. Eng.* 2021, 5524591 (2021).
3. Bai, X. & Zhu, P. Research on roof caving mechanism and influencing factors in inclined ore body caving mining. *Results Eng.* **22**, 102048 (2024).
4. Song, W., Yu, S., Rong, H., Jiao, H. & Xu, X. Study on the characteristic of overburden rock structure and support system of the Retraction channel in layered fully mechanized caving face. *Sci. Rep.* **14**, 1360 (2024).
5. He, M., Cheng, T., Qiao, Y. & Li, H. A. Review of rockburst: experiments, theories, and simulations. *J. Rock. Mech. Geotech. Eng.* **15**, 1312–1353 (2023).
6. Zhang, C., Canbulat, I., Hebblewhite, B. & Ward, C. R. Assessing coal burst phenomena in mining and insights into directions for future research. *Int. J. Coal Geol.* **179**, 28–44 (2017).
7. Fan, C., Li, S., Luo, M., Du, W. & Yang, Z. Coal and gas outburst dynamic system. *Int. J. Min. Sci. Technol.* **27**, 49–55 (2017).
8. Wang, C. & Cheng, Y. Role of coal deformation energy in coal and gas outburst: A review. *Fuel* **332**, 126019 (2023).

9. Lu, Z., Ju, W., Gao, F. & Du, T. Numerical analysis on the factors affecting post-peak characteristics of coal under uniaxial compression. *Int. J. Coal Sci. Technol.* **11**, 2 (2024).
10. Liu, H., Jing, H., Yin, Q., Meng, Y. & Zhu, G. Effect of bedding plane on mechanical properties, failure mode, and crack evolution characteristic of bedded Rock-Like specimen. *Theor. Appl. Fract. Mec.* **123**, 103681 (2023).
11. Khalili, M., Fahimifar, A. & Shobeiri, H. The effect of bedding planes on the bending strength of Rock-Like material and evaluation of the crack propagation mechanism. *Theor. Appl. Fract. Mec.* **127**, 104061 (2023).
12. Lu, Z. et al. Experimental study on anisotropic characteristics of impact tendency and failure model of hard coal. *Chin. J. Rock. Mech. Eng.* **38**, 757–768 (2019).
13. Wang, X. et al. Effects of anisotropy on strength and deformability of anthracite under high confinement. *Rock. Mech. Rock. Eng.* **56**, 2157–2183 (2023).
14. Wang, X. et al. Energy evolution of anthracite considering anisotropy under high confining pressure: an experimental investigation. *Rock. Mech. Rock. Eng.* **56**, 6735–6759 (2023).
15. Sun, Z. et al. Effect of size and anisotropy on mode I fracture toughness of coal. *Theor. Appl. Fract. Mec.* **129**, 104170 (2024).
16. Huang, L., Li, B., Li, C., Wu, B. & Wang, J. Research on anisotropic characteristics and energy damage evolution mechanism of bedding coal under uniaxial compression. *Energy* **301**, 131659 (2024).
17. Zhou, J. et al. Loading Rate and Bedding Plane Coupled Effect Study On Coal Failure Under Uniaxial Compression: Acoustic Emissions and Energy Dissipation Analysis. *Geofluids*. 2022, 9028178 (2022).
18. Zhao, C. et al. Mechanical responses and failure characteristics of longmaxi formation shale under Real-Time high temperature and high-Stress coupling. *Eng. Fail. Anal.* **152**, 107490 (2023).
19. Qiao, C., Song, Z., Wang, Y., Tannant, D. & Li, C. Fractures and acoustic emission features of Non-Persistent jointed rocks subjected to Freeze-Thaw-Compression load: experimental insights. *Rock. Mech. Rock. Eng.* **55**, 109–123 (2022).
20. Wang, C. et al. Mechanical properties and acoustic emission characteristics of deep hard coal after segmented High-Temperature treatment. *Sci. Rep.* **13**, 1134 (2023).
21. Xie, Y., Hou, M. Z. & Li, C. Anisotropic characteristics of acoustic emission and the corresponding multifractal spectrum during progressive failure of shale under Cyclic loading. *Int. J. Rock. Mech. Min.* **165**, 105364 (2023).
22. Liu, S. et al. Bedding Effect On the Deformation: Damage Differentiation of Coal Mass. *Shock Vib.* 2022, 3916921 (2022).
23. Liu, J., Yang, M., Wang, D. & Zhang, J. Different bedding loaded coal mechanics properties and acoustic emission. *Environ. Earth Sci.* **77**, 322 (2018).
24. Song, H., Zhao, Y., Elsworth, D., Jiang, Y. & Wang, J. Anisotropy of acoustic emission in coal under the uniaxial loading condition. *Chaos Soliton Fract.* **130**, 109465 (2020).
25. Zhang, S. W., Shou, K. J., Xian, X. F., Zhou, J. P. & Liu, G. J. Fractal characteristics and acoustic emission of anisotropic shale in Brazilian tests. *Tunn. Undergr. Sp. Tech.* **71**, 298–308 (2018).
26. Chai, Y. et al. Experimental investigation into damage and failure process of Coal-Rock composite structures with different roof lithologies under Mining-Induced stress loading. *Int. J. Rock. Mech. Min.* **170**, 105479 (2023).
27. Song, D., Wang, E., Li, Z., Liu, J. & Xu, W. Energy dissipation of coal and rock during damage and failure process based on Emr. *Int. J. Min. Sci. Technol.* **25**, 787–795 (2015).
28. Gao, Y. et al. Loaded failure characteristics of anthracite derived from microwave irradiation: acoustic emission evaluation. *Rock. Mech. Rock. Eng.* **56**, 8809–8831 (2023).
29. Ohno, K. & Ohtsu, M. Crack classification in concrete based on acoustic emission. *Constr. Build. Mater.* **24**, 2339–2346 (2010).
30. Yu, B., Liang, J. & Ju, J. W. Classification method for crack modes in concrete by acoustic emission signals with Semi-Parametric clustering and support vector machine. *Measurement* **244**, 116474 (2025).
31. Ding, Z. et al. Research On Rock Crack Classification Based On Acoustic Emission Waveform Feature Extraction Technology. *Lithosphere* 2022, 5804064 (2022).
32. Han, P., Zhao, Y., Zhang, C. & Wang, X. Progressive damage characteristic and microscopic weakening mechanism of coal under Long-Term soaking. *Rock. Mech. Rock. Eng.* **56**, 7861–7881 (2023).
33. Gutenberg, B. & Richter, C. F. Frequency of earthquakes in California. *B Seismol. Soc. Am.* **34**, 185–188 (1944).
34. Dong, L., Zhang, L., Liu, H., Du, K. & Liu, X. Acoustic emission B value characteristics of granite under true triaxial stress. *Mathematics* **10**, 10030451 (2022).
35. Chajed, S. & Singh, A. Acoustic emission (AE) based damage quantification and its relation with Ae-Based micromechanical coupled damage plasticity model for intact rocks. *Rock. Mech. Rock. Eng.* **57**, 2581–2604 (2024).
36. Jiang, T., Chen, B., Bai, J., Liu, B. & Chen, M. Improving mechanism for recycling efficiency of ceramic construction solid waste and properties of composite backfill based on aggregate particle size distribution. *Constr. Build. Mater.* **436**, 136826 (2024).
37. Jiang, T., Cao, X., Duan, H. & Shu, K. Recycling efficiency mechanism of recycled concrete aggregate to improve the CO₂ uptake and anti-leakage properties of CO₂ sequestration functional backfills. *Constr. Build. Mater.* **458**, 139663 (2025).
38. Chen, S. et al. Influence of Cyclic wetting-drying on the mechanical strength characteristics of coal samples: A laboratory-scale study. *Energy Sci. Eng.* **7**, 3020–3037 (2019).
39. Jiang, T. et al. Deterioration evolution mechanism and damage constitutive model improvement of sandstone-coal composite samples under the effect of repeated immersion. *Phys. Fluids* **36**, 056611 (2024).

Author contributions

Z. G. performed the laboratory experiment and drafted the manuscript. Y. Y. and Z.W. revised the manuscript.

Declarations

Competing interests

The authors declare no competing interests.

Additional information

Correspondence and requests for materials should be addressed to Y.Y.

Reprints and permissions information is available at www.nature.com/reprints.

Publisher's note Springer Nature remains neutral with regard to jurisdictional claims in published maps and institutional affiliations.

Open Access This article is licensed under a Creative Commons Attribution-NonCommercial-NoDerivatives 4.0 International License, which permits any non-commercial use, sharing, distribution and reproduction in any medium or format, as long as you give appropriate credit to the original author(s) and the source, provide a link to the Creative Commons licence, and indicate if you modified the licensed material. You do not have permission under this licence to share adapted material derived from this article or parts of it. The images or other third party material in this article are included in the article's Creative Commons licence, unless indicated otherwise in a credit line to the material. If material is not included in the article's Creative Commons licence and your intended use is not permitted by statutory regulation or exceeds the permitted use, you will need to obtain permission directly from the copyright holder. To view a copy of this licence, visit <http://creativecommons.org/licenses/by-nc-nd/4.0/>.

© The Author(s) 2025